

Analysis of a Two-degree-of-freedom Beam for Rotational Piezoelectric Energy Harvesting

Xiang-Yu Li, I-Chie Huang, Wei-Jiun Su*

Department of Mechanical Engineering, National Taiwan University, No. 1, Sec. 4, Roosevelt Rd., Taipei, 10617, Taiwan

Abstract

This study introduces a two-degree-of-freedom piezoelectric energy harvester designed to harness rotational motion. The harvester is built using a cut-out beam which enables the first two resonant frequencies to be located close to each other. A distributed continuous model is developed and validated with experimental results. As the beam undergoes significant displacement due to rotational excitations, the geometric nonlinearity arising from longitudinal displacement is considered in the model. Compared to previous literature, the simulation results are much more precise for rotational energy harvesting. It is observed that as the rotating speed increases, the increased centrifugal force causes the first resonant frequency to rise while the second resonant frequency decreases. This study explores the potential to expand the bandwidth of the harvester using two types of nonlinear external force, namely mechanical stoppers and magnetic force. The results indicate that the proposed harvester can broaden the bandwidth by 1.17 Hz and 0.33 Hz at the first and second resonance frequencies, respectively, by using a stopper on the main beam.

Keywords: geometric nonlinearity, rotational motion, piezoelectric energy harvester, multimodal, mode veering, nonlinear force

1. Introduction

The cantilevered beam is a widely used structure for piezoelectric energy harvesting due to its simplicity. Extensive theory models and research have been carried out on conventional cantilevered piezoelectric energy harvesters. Erturk and Inman et al. [1, 2] proposed a theoretical model of a cantilevered energy harvester under base excitations and validated it with experimental results. This model underestimates the deflection and overestimates the natural frequencies due to the neglect of transverse shear deformation and the rotary inertia effects [3]. Rotational energy harvesting has the potential for a variety of applications, including vehicle suspensions, engine/machinery mounts, etc. However, compared to base excitation, rotational excitation imposes a significant axial load on the beam and causes non-negligible lateral deflection. Yigit et al. [4] derived fully coupled nonlinear motion equations for a rotating cantilevered beam and investigated the impact of coupling terms on vibration waveforms using linearized analysis and numerical solutions. Gu and Livermore et al. [5] verified the effect of centrifugal force in the rotating environment on the system. After optimization, the harvester's resonant frequency closely matches the rotation frequency over a wide frequency range ranging from 4 to 16.2 Hz. Khameneifar et al. [6, 7] developed a rotational energy harvester specifically for a hub-type rotational system. Hsu et al. [8] employed

finite element analysis to study a rotating cantilevered beam with an end mass and validated their results with experimental data. Mei et al. [9] uncovered the underlying mechanism of the centrifugal force acting on the PEH and demonstrated its impact on dynamic performances. Su et al. [10] explored three orientations, namely inward, outward, and tilted configurations, for a horizontal rotational piezoelectric energy harvester. According to the findings, adjusting the installation distance and tilt angle can match the system's resonant frequency with the excitation frequency. Turhan and Bulut et al. [11] investigated nonlinear bending vibrations of a rotating beam using Galerkin's method and conducted perturbation analyses to determine amplitude-dependent natural frequencies and frequency responses.

Linear energy harvesters only work efficiently when the excitation frequency is close to the natural frequencies, limiting harvesting bandwidth. To address this challenge, recent REH studies have focused on broadening the bandwidth of rotational energy harvesting through methods such as mechanical structure optimization [12-14], external circuitry [15, 16], nonlinear methods, multi-modal techniques, and hybrid systems methods[17]. Nonlinear methods, on the one hand, can optimize rotational energy harvesting through the system's inherent characteristics, such as the stress hardening/softening nonlinearity effect in rotational systems. Mei et al. [18] propose an inverse harvester that exhibits a centrifugal softening effect. The output voltage is significantly enhanced over the speed range of 75-120 rpm (1.2-2 Hz). On the other hand, nonlinear forces can be introduced externally, such as impact forces (contact execution)[19-21] or magnetic forces (non-contact execution).

Magnetic force is a common method for introducing nonlinearity to rotational systems. Kan et al. [22] presented a novel cantilevered piezoelectric energy harvester using repulsive magnets for rotary motion. Fan et al. [23] reported an innovative vibration-to-rotation conversion mechanism utilizing a new plectrum design for converting ambient vibrations to uni-directional and high-speed rotation, resulting in a high output power of 4 mW under a harmonic vibration of 0.4 g at 8.6 Hz. Rui et al. [24] proposed a three-beam impact energy harvester that demonstrated low-frequency band, wide-frequency band, and parameter insensitivity characteristics, enhancing harvesting efficiency and making it suitable for use in low-frequency rotational structures with limited volume. In addition to the studies above, the latest research on rotational piezoelectric energy harvesting with magnetic forces often comes with multi-stable systems and focuses on magnet arrays. Mono-stable[25] and bi-stable [26-28] are the primary, it quickly expands investigations into more stable states. Kan et al. [29] present a tunable rotational energy harvester with magnetic interaction force to enhance the robustness, excited by rotational magnets. Mei et al. [30] investigated the performance of a tri-stable piezoelectric energy harvester in rotational motion. Mei et al. [31] propose a quad-stable piezoelectric energy harvester that combines the advantages of lower potential barriers and time-varying potential wells.

Moreover, impulse force is another commonly used nonlinear force for rotational energy harvesting. Rui et al. [32] examined a rotational energy harvester with limiters and discovered that stiffness has little impact on the limiting effect. Fang et al. [32, 33] analyzed a rotational impact energy harvester that was composed of a centrifugal-softening driving beam. They found that the centrifugal softening effect can amplify the relative motion and increase the impact force, thus improving output power at low rotational frequencies. Machado [20] proposed a low-frequency rotational piezoelectric energy harvester that can

operate out of resonance with the incorporation of a flexible stop.

Multi-modal technology has been widely studied as a promising method for wideband energy harvesting. However, few researches have been done on rotational energy harvesting due to the shortcomings of high resonance frequencies and complex motion modes. Yu et al. [34] propose a novel rotating-DOF piezoelectric energy harvester to efficiently achieve tri-modal vibration energy harvesting in low-frequency environments, particularly at its first-order resonant frequency, down to 12.65 Hz. Raja et al. [35] utilize a multi-mode structure consisting of a reversed exponentially tapered beam and six branched beams attached with a flange to the free end of the primary beam.

Hybrid systems methods comprehensively utilize different configurations to achieve better output using meticulous design. A trapezoid piezoelectric cantilever beam excited by a magnet fixed on the revolving plate is proposed to improve the output [36]. Another study by Fang et al. [37] introduces an auxetic centrifugal softening impact energy harvester that increases the peak power by 200.45% at 3.5 Hz. Xing et al.[38] proposes a gravity-based rotational hybrid energy harvester that utilizes a bi-stable mechanism, and achieves one order of magnitude higher performance than other energy harvesters. Approaches that hybridize different mechanisms such as electrostatic[39] and electromagnetic[40] are not within the scope of this discussion.

The aforementioned literature barely achieved the application of both multi-modal and nonlinear methods. In this study, we design a two-degree-of-freedom rotational energy harvester to improve low-frequency energy harvesting with two peaks. Moreover, the bandwidth has the potential to be further enhanced by the introduction of impulse and magnetic forces.

2. Design and modeling

As shown in Fig. 1, the proposed design is composed of a cut-out beam, a piezoelectric layer, and two tip masses. The cut-out beam is divided into four sections, with the main beam fixed on the rotational base. The cut-out structure brings the beam a small width and the effects of torsion modal can be ignored. The piezoelectric layer is fixed at the second section of the main beam, while the two tip masses are mounted at the free end of the main beam and auxiliary beam. In the subsequent discussion, the term "main beam" refers to the range covering L_1 to L_3 , while the auxiliary beam covers L_4 . The local coordinates of the PEH are depicted in Fig. 2, where x_i denotes the longitudinal position of the beam along the neutral axis.

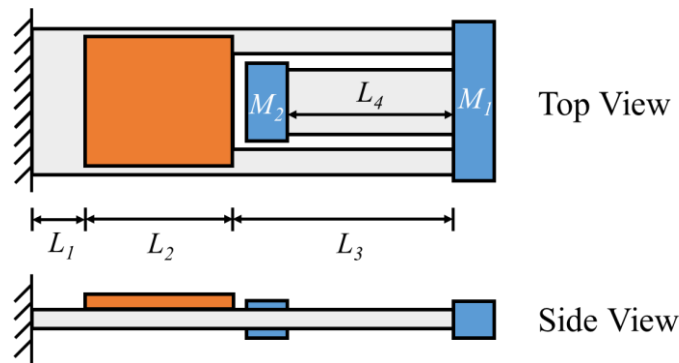


Fig. 1 Schematics of the rotational two-degree-of-freedom PEH.

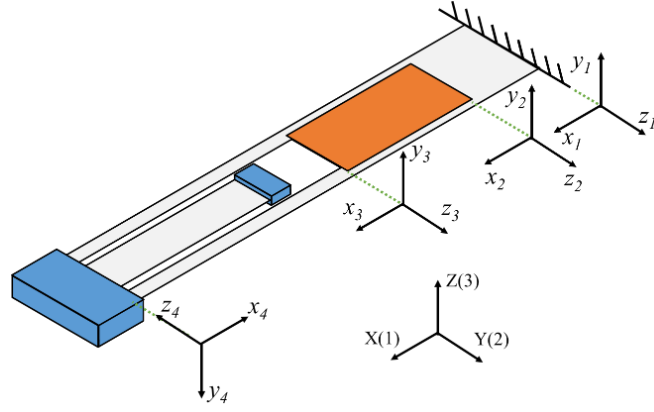


Fig. 2 The local coordinates of the rotational two-degree-of-freedom PEH.

This study aims to investigate the effects of stoppers and magnetic force on the performance of the PEH. The schematics of the PEHs equipped with stoppers and magnets are shown in Fig. 3. The stopper is a cantilever beam with a tip mass attached to it for collision. The fixed magnet is mounted directly below the magnet of the cut-out beam.

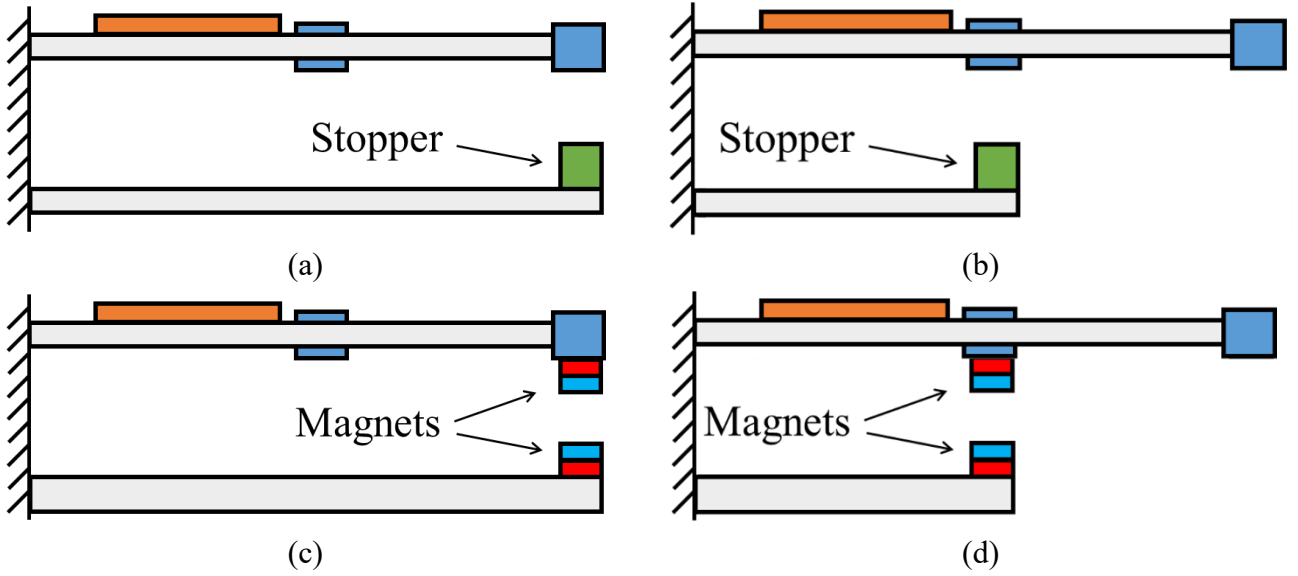


Fig. 3 Side views of the rotational PEHs with a stopper (a) on the main beam and (b) on the auxiliary beam; with magnets (c) on the main beam and (d) on the auxiliary beam.

2.1. PEH with Geometric Nonlinearity

When subjected to rotational excitations, the transverse displacement of the PEH is substantial due to the large excitation force caused by gravity. Therefore, this paper developed a theoretical model that considers the longitudinal displacement of the beam. The geometrical nonlinearity resulting from the longitudinal displacement can be mathematically expressed as:

$$u_i(x_i, t) = \int_0^{x_i} 1 - \sqrt{1 - w_i'^2(s, t)} ds \approx \int_0^{x_i} w_i'^2(s, t) ds \quad (1)$$

where w is the transverse displacement and u is the longitudinal displacement. Consider a unit element as shown in Fig. 4. The angle α and the curvature κ during vibration can be determined using eqns.(2)-(5):

$$\sin(\alpha(x_i, t)) = w'_i(x_i, t) \quad (2)$$

$$\cos(\alpha(x_i, t)) = 1 - \frac{1}{2} w_i'^2(x_i, t) \quad (3)$$

$$\alpha(x_i, t) \approx w'_i(x_i, t) \quad (4)$$

$$\kappa = \frac{d\alpha}{ds} \approx \frac{w''}{1 - \frac{1}{2} w'^2} \approx w'' + \frac{1}{2} w'' w'^2 \quad (5)$$

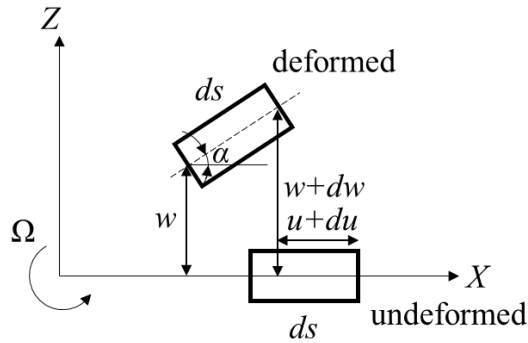


Fig. 4 Schematics of a beam element

The moment balance can be expressed as eqn.(6):

$$dM_i - P_i \times dw_i + Q_i \times dx_i = m_i I_i dx_i \ddot{\theta} \quad (6)$$

where Q_i is the shear force, I is the area moment of inertia, M is the bending moment, θ is the deviation angle of a beam unit, m_i is the linear density of the beam, the centrifugal force P_i refers to

$$P_i = f c_i \Omega^2 = \left[m_i \int_s^{L_i} (x_i + R_i) dx_i + M t_i (L_i + R_i) \right] \Omega^2 \quad (7)$$

where $f c_i$ refers to the centrifugal coefficient, it is only used to simplify expressions, Ω is the rotation speed of the environment; R is the radius of rotation of the fixed end, $R_1=R$, $R_2=R+L_1$, $R_3=R+L_1+L_2$, $R_4=(R+L_1+L_2+L_3)$ are the mathematical radius of rotation, $M t_1=M t_2=0$, $M t_3=M_1$, $M t_4=M_2$ are mathematical mass at the end of different beam sections. Then the shear force Q_i in the transverse direction can be expressed instead as:

$$Q_i = -Y I_i \left[w_i'''(x_i, t) + \frac{1}{2} w_i'''(x_i, t) w_i'^2(x_i, t) + w_i'(x_i, t) w_i''^2(x_i, t) \right] + P_i w_i'(x_i, t) + m_i I_i \frac{\partial^2}{\partial t^2} w_i'(x_i, t) \quad (8)$$

where $Y I_i$ is the bending stiffness of different beam sections.

Integrate the axial force balance of a beam unit (44) (Appendix A) from x_i to L_i and bring it into

the lateral force balance on boundaries of different beam sections (46) (Appendix B), then the equation for the relationship between F_i and Q_i can be expressed as:

$$\left\{ \begin{array}{l} F_i(x_i, t) = \frac{1}{\cos(\alpha_i(x_i, t))} \left\{ Q_i \sin(\alpha_i(x_i, t)) + [fc_i(x_i) + fc_{i+1}(0)]\Omega^2 \right. \\ \left. - [fg_i(x_i) - fg_{i+1}(0)]\cos\Omega t + fn_i(x_i, t) + fn_{i+1}(0, t) \right\} \quad i=1,2 \\ F_3(x_3, t) = \frac{1}{\cos(\alpha_3(x_3, t))} \left\{ Q_3 \sin(\alpha_3(x_3, t)) + [fc_3(x_3) - fc_4(0)]\Omega^2 \right. \\ \left. - [fg_3(x_3) + fg_4(0)]\cos\Omega t + fn_3(x_3, t) - fn_4(0, t) \right\} \\ F_4(x_4, t) = \frac{1}{\cos(\alpha_4(x_4, t))} [Q_4 \sin(\alpha_4(x_4, t)) + fc_4(x_4)\Omega^2 + fg_4(x_4)\cos\Omega t + fn_4(x_4, t)] \end{array} \right. \quad (9)$$

where $fc_i(x_i)\Omega^2$ is the centrifugal force coefficient, $fg_i(x_i)\cos\Omega t$ is the axial component of gravity coefficient, and $fn_i(x_i, t)$ is the axial component of inertia coefficient.

$$fc_i(x_i) = \left[m_i \int_s^{L_i} (x_i + R_i) dx_i + Mt_i (L_i + R_i) \right] \quad (10)$$

$$fg_i(x_i) = [(L_i - x_i)m_i + Mt_i] g \quad (11)$$

$$fn_i(x_i, t) = m_i \int_s^{L_i} \left[\frac{\partial^2 u_i(x_i, t)}{\partial t^2} - \Omega^2 u_i(x_i, t) \right] ds + Mt_i \left[\frac{\partial^2 u_i(L_i, t)}{\partial t^2} - \Omega^2 u_i(L_i, t) \right] \quad i=1,2,3,4 \quad (12)$$

Consider bringing the eqns.(8)-(9) into the lateral force balance equation (47) (Appendix B). After simplification, the forced vibration equation of the cut-out beam, considering the balance of axial displacement and axial force, is obtained:

$$\left\{ \begin{array}{l} YI_i \left\{ w_i''''(x_i, t) + \left[w_i'(x_i, t) (w_i'(x_i, t) w_i''(x_i, t))' \right]' \right\} + m_i \left[\frac{\partial^2 w_i(x_i, t)}{\partial t^2} - \Omega^2 w_i(x_i, t) \right] \\ - AF_i w_i''(x_i, t) = m_i g \sin \Omega t \\ YI_4 \left\{ w_4''''(x_4, t) + \left[w_4'(x_4, t) (w_4'(x_4, t) w_4''(x_4, t))' \right]' \right\} + m_4 \left[\frac{\partial^2 w_4(x_4, t)}{\partial t^2} - \Omega^2 w_4(x_4, t) \right] \\ - AF_4 w_4''(x_4, t) = -m_4 g \sin \Omega t \end{array} \right. \quad i=1,2,3 \quad (13)$$

where the axial force term AF refers to:

$$\left\{ \begin{array}{l} AF_i(x_i, t) = [fc_i(x_i) + fc_{i+1}(0)]\Omega^2 - [fg_i(x_i) - fg_{i+1}(0)]\cos\Omega t + [fn_i(x_i, t) + fn_{i+1}(0, t)] \quad i=1,2 \\ AF_3(x_3, t) = [fc_3(x_3) - fc_4(0)]\Omega^2 - [fg_3(x_3) + fg_4(0)]\cos\Omega t + [fn_3(x_3, t) - fn_4(0, t)] \\ AF_4(x_4, t) = fc_4(x_4)\Omega^2 + fg_4(x_4)\cos\Omega t + fn_4(x_4, t) \end{array} \right. \quad (14)$$

2.2. Modal Analysis

Ignoring the damping, the external force, and the nonlinear terms, the undamped free vibration of the beam can be rewritten as:

$$\begin{cases} YI_1 w_1''''(x_1, t) - [fc_1(x_1) + fc_{2+1}(0)] \Omega^2 w_1''(x_1, t) + m_1 \left(\frac{\partial^2 w_1(x_1, t)}{\partial t^2} - \Omega^2 w_1'(x_1, t) \right) = 0 & i=1, 2 \\ YI_3 w_3''''(x_3, t) - [fc_3(x_3) - fc_4(0)] \Omega^2 w_3''(x_3, t) + m_3 \left(\frac{\partial^2 w_3(x_3, t)}{\partial t^2} - \Omega^2 w_3'(x_3, t) \right) = 0 \\ YI_4 w_4''''(x_4, t) - fc_4(x_4) \Omega^2 w_4''(x_4, t) + m_4 \left(\frac{\partial^2 w_4(x_4, t)}{\partial t^2} - \Omega^2 w_4'(x_4, t) \right) = 0 \end{cases} \quad (15)$$

The transverse displacement w_i can be expressed as eqn.(16)

$$w_i(x_i, t) = \sum_{j=1}^n \phi_{ij}(x_i) \eta_j(t) \quad (16)$$

where ϕ_{ij} is the mode shape function, η_j is the temporal function, and the subscript j represents the mode number. To complete the calculation, $fc_i(x_i)$ is converted to RMS value by using eqn.(17):

$$\begin{cases} \overline{fc_1} = \sqrt{\frac{\int_0^{L_1} [fc_1(x_1) + fc_{2+1}(0)]^2 dx_1}{L_1}} & i=1, 2 \\ \overline{fc_3} = \sqrt{\frac{\int_0^{L_3} [fc_3(x_3) - fc_4(0)]^2 dx_3}{L_3}} \\ \overline{fc_4} = \sqrt{\frac{\int_0^{L_4} fc_4(x_4)^2 dx_4}{L_4}} \end{cases} \quad (17)$$

The model shape function can be expressed as:

$$\phi_{ij}(x_i) = A_{ij} \cosh(a_{ij} x_i) + B_{ij} \sinh(a_{ij} x_i) + C_{ij} \cos(b_{ij} x_i) + D_{ij} \sin(b_{ij} x_i) \quad (18)$$

where A_{ij} , B_{ij} , C_{ij} , and D_{ij} will be determined by the boundary and continuous conditions. The boundary and continuous conditions of the rotational PEH are listed in Eqns. (19)-(30).

$$w_1(0, t) = 0 \quad (19)$$

$$w_1'(x_1, t) \Big|_{x_1=0} = 0 \quad (20)$$

$$w_i(L_i, t) = w_{i+1}(0, t) \quad i=1, 2 \quad (21)$$

$$w_i'(x_i, t) \Big|_{x_i=L_i} = w_{i+1}'(x_{i+1}, t) \Big|_{x_{i+1}=0} \quad i=1, 2 \quad (22)$$

$$YI_i w_i''(x_i, t) \Big|_{x_i=L_i} = YI_{i+1} w_{i+1}''(x_{i+1}, t) \Big|_{x_{i+1}=0} \quad i=1, 2 \quad (23)$$

$$\begin{aligned}
& YI_i \left[w_i'''(x_i, t) \left(w_i'(x_i, t) \right)^2 + \left(w_i''(x_i, t) \right)^2 w_i'(x_i, t) + w_i'''(x_i, t) \right] - AF_i(x_i) w_i'(x_i, t) + Mt_i g \sin \Omega t \\
& - Mt_i \left[\frac{\partial^2 w_i(x_i, t)}{\partial t^2} - \Omega^2 w_i(x_i, t) \right] \Big|_{x_i=L_i} = YI_{i+1} w_{i+1}''(x_{i+1}, t) - AF_{i+1}(x_{i+1}) w_{i+1}'(x_{i+1}, t) \Big|_{x_{i+1}=0} \quad i=1, 2 \quad (24)
\end{aligned}$$

$$w_3(L_3, t) = -w_4(0, t) \quad (25)$$

$$w_3'(x_3, t) \Big|_{x_3=L_3} = w_4'(x_4, t)_{x_4=0} \quad (26)$$

$$YI_3 w_3''(x_3, t) \Big|_{x_3=L_3} + I_{M_3} \frac{\partial^2}{\partial t^2} w_3'(x_3, t) \Big|_{x_3=L_3} = YI_4 w_4''(x_4, t) \Big|_{x_4=0} \quad (27)$$

$$\begin{aligned}
& YI_3 \left[w_3'''(x_3, t) w_3'^2(x_3, t) + w_3''^2(x_3, t) w_3'(x_3, t) + w_3'''(x_3, t) \right] - AF_3(x_3) w_3'(x_3, t) \\
& + Mt_3 g \sin \Omega t - Mt_3 \left[\frac{\partial^2 w_3(x_3, t)}{\partial t^2} - \Omega^2 w_3(x_3, t) \right] \Big|_{x_3=L_3} = -YI_4 w_4''(x_4, t) + AF_4(x_4) w_4'(x_4, t) \Big|_{x_4=0} \quad (28)
\end{aligned}$$

$$\begin{aligned}
& YI_4 \left[w_4'''(x_4, t) w_4'^2(x_4, t) + \left(w_4''(x_4, t) \right)^2 w_4'(x_4, t) + w_4'''(x_4, t) \right] \\
& - AF_4 w_4'(x_4, t) - Mt_4 g \sin \Omega t - Mt_4 \left[\frac{\partial^2 w_4(x_4, t)}{\partial t^2} - \Omega^2 w_4(x_4, t) \right] = 0 \quad (29)
\end{aligned}$$

$$w_4''(x_4, t) \Big|_{x_4=L_4} = 0 \quad (30)$$

where rotational inertia of beams I_{Mi} can be represented as:

$$I_{M_i} = M_i I_i \ddot{\alpha}_i(x_i, t) \Big|_{x_i=L_i} \approx M_i I_i \frac{\partial^2}{\partial t^2} w_i'(x_i, t) \Big|_{x_i=L_i} \quad (31)$$

Eqns.(19)-(30) can be rearranged in the form of a matrix multiply a vector as:

$$M_{16 \times 16} \cdot \begin{bmatrix} A_{ij} \\ \vdots \\ D_{ij} \end{bmatrix} = \begin{bmatrix} 0 \\ \vdots \\ 0 \end{bmatrix}, \quad (32)$$

The natural frequencies can be obtained when the determinant of M is equal to zero. The mode shape function is mass-normalized according to eqn.(33).

$$\left\{ \begin{aligned} & \sum_{i=1}^4 \left\{ \int_0^{L_i} \phi_{ik}'(x_i) m_i \phi_{ij}(x_i) dx_i + \phi_{ik}(x_i) M t_i \phi_{ij}(x_i) \Big|_{x_i=L_i} + \left[\phi_{ik}'(x_i) I_{M_i} \phi_{ij}'(x_i) dx_i \right] \right\} = \delta_{jk} \\ & \sum_{i=1}^2 \left\{ \int_0^{L_i} \phi_{ik}'(x_i) [f c_i(x_i) + f c_{i+1}(0)] \Omega^2 \phi_{ij}'(x_i) dx_i \right\} \\ & + \int_0^{L_3} \phi_{3k}'(x_3) [f c_3(x_3) - f c_4(0)] \Omega^2 \phi_{3j}'(x_3) dx_3 + \int_0^{L_4} \phi_{4k}'(x_4) f c_4(x_4) \Omega^2 \phi_{4j}'(x_4) dx_4 \quad \delta_{jk} = \begin{cases} 0 & \text{if } j = k \\ 1 & \text{if } j \neq k \end{cases} \quad (33) \\ & + \sum_{i=1}^4 \left\{ \int_0^{L_i} \phi_{ik}''(x_i) Y I_i \phi_{ij}''(x_i) dx_i + \left[\phi_{ik}'(x_i) I_{M_i} \phi_{ij}''(x_i) dx_i \right] \right\} \\ & - \Omega^2 \left[\int_0^{L_i} \phi_{ik}(x_i) m_i \phi_{ij}(x_i) dx_i + \phi_{ik}(x_i) M t_i \phi_{ij}(x_i) \Big|_{x_i=L_i} \right] \right\} = \omega_j^2 \delta_{jk}
\end{aligned} \right.$$

The equation of motion of the PEH is obtained by using the orthogonal equations above,

$$\begin{aligned}
\ddot{\eta}_i(t) + \omega_j^2 \left(1 - \frac{K g_{jk} \cos \Omega t}{K b_{jk} + (K s_{jk} - M b_{jk}) \Omega^2} \right) \eta_i(t) + \left(R s_{jk} - \frac{1}{2} \Omega^2 K n_{jk} \right) \eta_i^3(t) \\
+ K n_{jk} \left[\eta_i(t) \dot{\eta}_i^2(t) + \eta_i^2(t) \ddot{\eta}_i(t) \right] = F_j \sin \Omega t
\end{aligned} \quad (34)$$

where $M b_{jk}$, $K b_{jk}$, $K s_{jk}$, $K g_{jk}$, $R s_{jk}$, $K n_{jk}$, and F_j represent the terms of quality, rigidity, stress hardening, gravitational force, rigidity nonlinearity, inertia nonlinearity and external force. The details of these terms can be found in Appendix C. The first two modes are investigated in this study. Assuming that the first two modes are perfectly orthogonal, only the principal diagonal terms of these matrices are nonzero and we

transform those terms from 2×2 matrices to 2×1 vectors, for example $\begin{bmatrix} K b_1 \\ K b_2 \end{bmatrix} = \begin{bmatrix} K b_{11} \\ K b_{22} \end{bmatrix}$. Finally, the damp-

ing, excitation force and electromechanical coupling are considered in the model and the governing equation of the PEH can be rewritten as:

$$\begin{aligned}
\ddot{\eta}_i(t) + 2 \zeta_i \omega_i \dot{\eta}_i(t) + (\omega_i^2 - K g_i \cos \Omega t) \eta_i(t) + \left(R s_i - \frac{1}{2} \Omega^2 K n_i \right) \eta_i^3(t) \quad i = 1, 2 \\
+ K n_i \left[\eta_i(t) \dot{\eta}_i^2(t) + \eta_i^2(t) \ddot{\eta}_i(t) \right] + \theta_i v(t) = F_i \sin \Omega t
\end{aligned} \quad (35)$$

where ζ_i is the mechanical damping ratio and F_i is the normalized excitation force. θ_i is the electro-mechanical coupling coefficient and can be represented as:

$$\theta_i = - \frac{e_{31} Y_p b_p (h_c^2 - h_b^2)}{h_p} \phi_i'(x_2)_{x_2=L_p} \quad (36)$$

where Y_p , b_p , h_p , and e_{31} are the Young's modulus, width, thickness and piezoelectric constant of the piezoelectric layer; h_b is the distance from the neutral axis of beam to the bottom surface of the piezoelectric layer; h_c is the distance from the neutral axis of beam to the top surface of the piezoelectric layer.

The equation of the circuit can be represented as eqn.(37).

$$C_p \dot{v}(t) + \frac{1}{R_l} v(t) + \sum_{i=1}^2 \theta_i \dot{\eta}_i(t) = 0 \quad (37)$$

where v is the output voltage, R_l is the load resistance, and C_p is capacitance.

The mode shapes of the PEH under the vibration of rotating can be found in Fig. 5. The equivalent circuit is shown in Fig. 6.

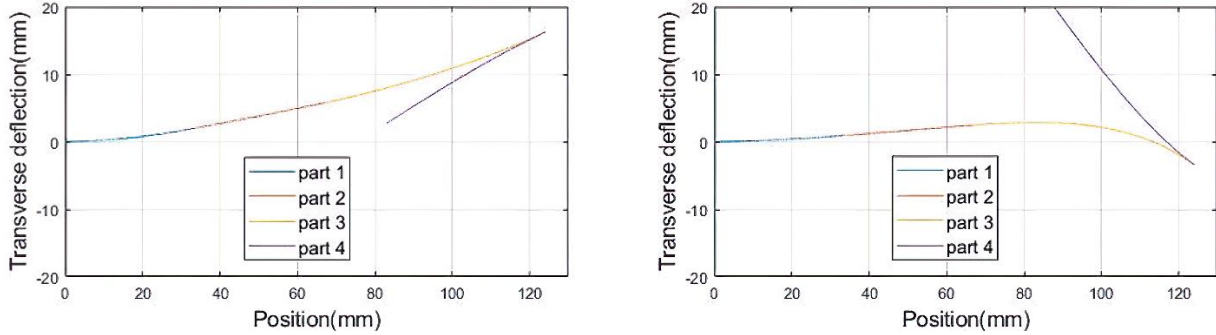


Fig. 5 Mode shapes of the PEH (a) Mode shape 1 (b) Mode shape 2.

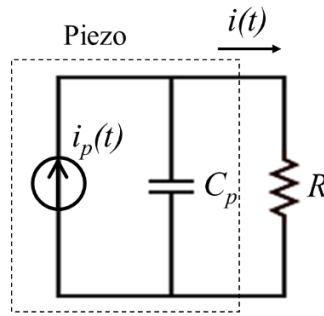


Fig. 6 The equivalent circuit of the PEH.

The relationship between the driving frequency and the natural frequency of the PEH is depicted in Fig. 7, where mode veering is observed at about 15 Hz. The mode shapes of the two modes are shown in Fig. 8. Near the frequency of the mode veering, the mode shape of each mode changes. Although mode 1 always resonates at a lower frequency than mode 2, mode shape 1 can resonate before/near/after mode shape 2.

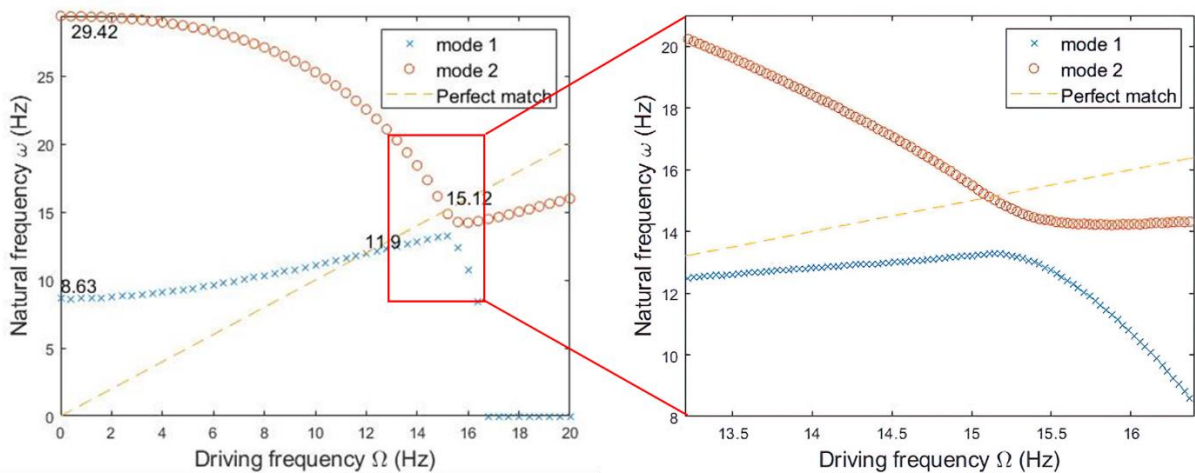


Fig. 7 The first two natural frequencies vs. the driving frequency

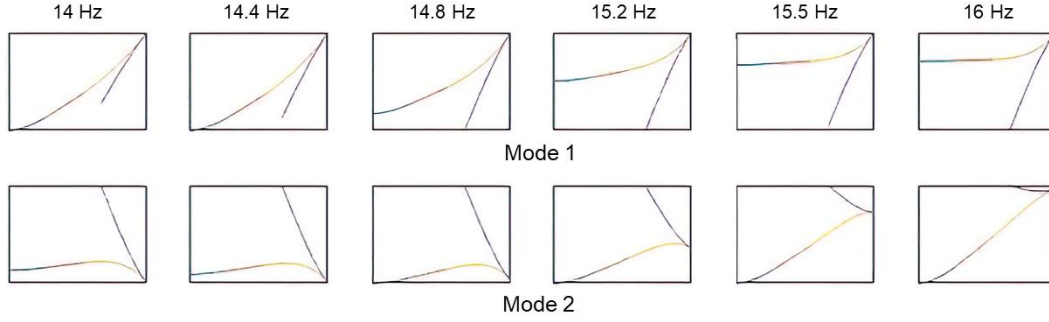


Fig. 8 Mode shapes of mode 1 and 2

2.3. Model of the PEH with stoppers

In this chapter, the impulse force of a stopper is introduced as an external force. Two basic situations are considered: a collision between the main beam and the auxiliary beam. The stopper is developed based on the Euler-Bernoulli beam, which has a stiffness much higher than that of the cut-out beam. The displacement of the main beam and auxiliary beam of the PEH is limited by a tip mass in each stopper. In the model, the impact is considered as a completely inelastic collision and the motion function of a stopper can transform into the form of MCK. Each impact force can be represented as a lumped parameter model (LPM):

$$\left. \begin{aligned}
 F_{imp1} &= \begin{cases} \frac{2\zeta_{st}\omega_{st}}{[\phi_{st}(L_{st})]^2} \left[\sum_{i=1}^2 \phi_{3i}(L_3) \dot{\eta}_i(t) - \phi_{st}(L_{st}) \dot{\eta}_{st}(t) \right] & \text{if } y_{rel} \leq -d_1 \\
 + \frac{\omega_{st}^2}{[\phi_{st}(L_{st})]^2} \left[\sum_{i=1}^2 \phi_{3i}(L_3) \eta_i(t) - \phi_{st}(L_{st}) \eta_{st}(t) + d_1 \right] & \\
 0 & \text{if } y_{rel} > -d_1 \end{cases} \\
 F_{imp2} &= \begin{cases} \frac{2\zeta_{st}\omega_{st}}{[\phi_{st}(L_{st})]^2} \left[\sum_{i=1}^2 \phi_{4i}(L_4) \dot{\eta}_i(t) - \phi_{st}(L_{st}) \dot{\eta}_{st}(t) \right] & \text{if } y_{rel} \geq d_2 \\
 + \frac{\omega_{st}^2}{[\phi_{st}(L_{st})]^2} \left[\sum_{i=1}^2 \phi_{4i}(L_4) \eta_i(t) - \phi_{st}(L_{st}) \eta_{st}(t) - d_2 \right] & \\
 0 & \text{if } y_{rel} < d_2 \end{cases}
 \end{aligned} \right\} \quad (38)$$

where F_{imp1} and F_{imp2} represent the impact impulse that occurs when a stopper collides with the main and auxiliary beams, respectively. d represents the mathematical distance between the stopper and the PEH. $y_{rel}(t)$ represents the relative displacement between a stopper and the beam. By taking the magnetic force into account, the force balance can be rewritten, resulting in the forced vibration equation. Similarly, by normalizing the function, the electromechanical coupling equation can be expressed as eqn.(39).

$$\begin{cases}
\ddot{\eta}_i(t) + 2\zeta_i \omega_i \dot{\eta}_i(t) + (\omega_i^2 - Kg_i \cos \Omega t) \eta_i(t) + \left(Rs_i - \frac{1}{2} \Omega^2 Kn_i \right) \eta_i^3(t) \\
+ Kn_i \left[\eta_i(t) \dot{\eta}_i^2(t) + \eta_i^2(t) \ddot{\eta}_i(t) \right] + \theta_i v(t) + F_{imp_j} \phi_{j+2,i}(L_{j+2}) = F_i \sin \Omega t \\
\ddot{\eta}_{st}(t) + 2\zeta_{st} \omega_{st} \dot{\eta}_{st}(t) + \omega_{st}^2 \eta_{st}(t) = F_{st} \sin \Omega t \\
Cp\dot{v}(t) + \frac{1}{R_l} v(t) + \sum_{i=1}^2 \theta_i \dot{\eta}_i(t) = 0
\end{cases} \quad i=1,2; j=1,2 \quad (39)$$

where i is the mode of the PEH with stopper, j equals 1 when the stopper on the main beam and equals 2 when on the auxiliary beam

2.4. Model of the PEH with magnetic force

In this section, the magnetic force of the cubic magnets as an external force is introduced. Two basic situations are considered where the magnet is attached to the tip magnet of the main beam and the auxiliary beam. The magnet model is developed based on Akoun's model [41] of cubic magnets. Based on the model, the magnetic force can be expressed as eqn.(40).

$$F_{mag} = -\nabla U = \frac{B_1 B_2}{4\pi\mu_0} \sum_{i=0}^1 \sum_{j=0}^1 \sum_{k=0}^1 \sum_{l=0}^1 \sum_{m=0}^1 \sum_{n=0}^1 (-1)^{i+j+k+l+m+n} \varphi_{x,y,z}(u_{ij}, v_{kl}, w_{mn}, r) \quad (40)$$

where

$$\begin{cases}
\varphi_x = \frac{1}{2}(v^2 - w^2) \ln(r-u) + uv \ln(r-v) + wv \arctan\left(\frac{uv}{wr}\right) + \frac{1}{2} ru \\
\varphi_y = \frac{1}{2}(u^2 - w^2) \ln(r-v) + uv \ln(r-u) + wu \arctan\left(\frac{uv}{wr}\right) + \frac{1}{2} rv \\
\varphi_z = -wu \ln(r-u) - wv \ln(r-v) + uvarctan\left(\frac{uv}{wr}\right) - rw
\end{cases} \quad (41)$$

$$\begin{cases}
u_{ij} = \alpha + (-1)^j \frac{a_1}{2} - (-1)^i \frac{a_2}{2} \\
v_{kl} = \beta + (-1)^l \frac{b_1}{2} - (-1)^k \frac{b_2}{2} \\
w_{mn} = \gamma + (-1)^n \frac{c_1}{2} - (-1)^m \frac{c_2}{2}
\end{cases} \quad (42)$$

In this model, F_{mag} is in the direction of Z. By taking F_{mag} into account, the force balance can be rewritten, resulting in the free vibration of the PEH. Similarly, by normalizing the function, the electromechanical coupling equation can be expressed as eqn.(43).

$$\begin{cases}
\ddot{\eta}_i(t) + 2\zeta_i \omega_i \dot{\eta}_i(t) + (\omega_i^2 - Kg_i \cos \Omega t) \eta_i(t) + \left(Rs_i - \frac{1}{2} \Omega^2 Kn_i \right) \eta_i^3(t) \\
+ Kn_i \left[\eta_i(t) \dot{\eta}_i^2(t) + \eta_i^2(t) \ddot{\eta}_i(t) \right] + \theta_i v(t) + F_{mag} \phi_{j+2,i}(L_{j+2}) = F_i \sin \Omega t \\
Cp\dot{v}(t) + \frac{1}{R_l} v(t) + \sum_{i=1}^2 \theta_i \dot{\eta}_i(t) = 0
\end{cases} \quad i=1,2; j=1,2 \quad (43)$$

where i is the mode of the PEH with the magnets, j equals 1 when the magnet on the main beam, and j equals to 2 when the magnet on the auxiliary beam.

3. Experiment

As is shown in Fig. 9, the cut-out beam structure is a SK5 spring steel processed by WEDM, a PZT patch stuck to the second section of the cut-out beam. At both sides of the end of the main beam, two aluminum blocks (the mass 1) are fixed by two screws. Similarly, at both sides of the end of the auxiliary beam, two aluminum blocks (the mass 2) are fixed by one screw. A screw is fixed at the end of the stopper, which is adhered with hot melt adhesive to reduce energy loss during collision. A $5*5*5\text{ mm}$ cubic magnet and a $4*4*4\text{ mm}$ cubic magnet are fixed at the mass mounted at the end. Table 1 shows parameters of the prototype.

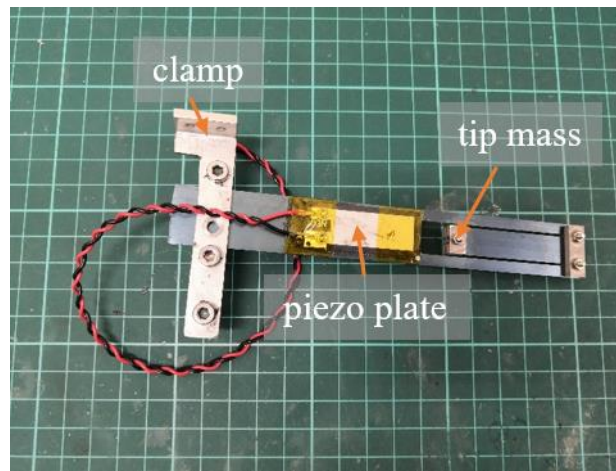


Fig. 9 Experimental equipment

Table 1 Parameters of the prototype.

Parameters	Symbol	Value
Radius of rotation of the PEH	R_l	30 mm
Radius of rotation of the stopper	R_{stA} / R_{stB}	90/60 mm
Length of the main beam	L	130 mm
Length of the first section of the main beam	L_1	33 mm
Length of the second section of the main beam	L_2	34 mm
Length of the third section of the main beam	L_3	57 mm
Length of the auxiliary beam	L_4	41 mm
Length of the mass	L_m	6 mm
Length of the stopper	L_{stA}/L_{stB}	70/55 mm
Length of the cubic magnet	L_{mag1}/L_{mag2}	3/4 mm
Length of the mass of the stopper	L_{mstA}/L_{mstB}	7 mm

Length of the PZT	L_e	34 mm
Young's modulus of the substrate	Y_s	193 GPa
Young's modulus of the piezoelectric material inside	Y_{pe}	4 GPa
Young's modulus of the PZT patch	Y_p	45 GPa
Young's modulus of the stopper	Y_{st}	193 GPa
Thickness of the substrate	h_s	0.3 mm
Thickness of the PZT patch	h_e	0.4 mm
Thickness of the stopper	h_{stA}/h_{stB}	1 mm
Width of the main beam	b_1	20 mm
Width of the auxiliary beam	b_2	12 mm
Width of the PZT patch	b_e	12 mm
Width of the stopper	b_{stA}/b_{stB}	20 mm
Density of the substrate	ρ_s	7930 kg/m ³
Density of the PZT patch	ρ_e	1780 kg/m ³
Density of the stopper beam	ρ_{st}	7930 kg/m ³
Weight of the mass at the end of the main beam	M_1	2.42 g/3.42 g
Weight of the mass at the end of the auxiliary beam	M_2	1.25 g/2.25 g
Weight of the mass at the end of the stopper beam	M_{stA}/M_{stB}	2.92 g/1.05 g
Capacitance (PZT)	C_p	1.38 nF
Piezoelectric constant (PZT)	d_{31}	-23e-12 C/N
Damping of mode 1 (L=130mm)	ζ_1	0.026-0.03
Damping of mode 2 (L=130mm)	ζ_2	0.028-0.035
Damping of mode 1 (L=140mm)	ζ_1	0.04
Damping of mode 2 (L=140mm)	ζ_2	0.045
Load resistance	R_l	1 M Ω

As is shown in Fig. 10, the controller increases and decreases the rotation speed at a constant rate, which results in an up-sweep and down-sweep. The controller inputs the speed signal with voltage into the motor and gives rotational excitation to the PEH. The voltage generated is transmitted to the oscilloscope through a wire, forming a waveform and voltage value. By recording the voltage of the oscilloscope at different speeds, the voltage data at different rotation rates can be obtained.

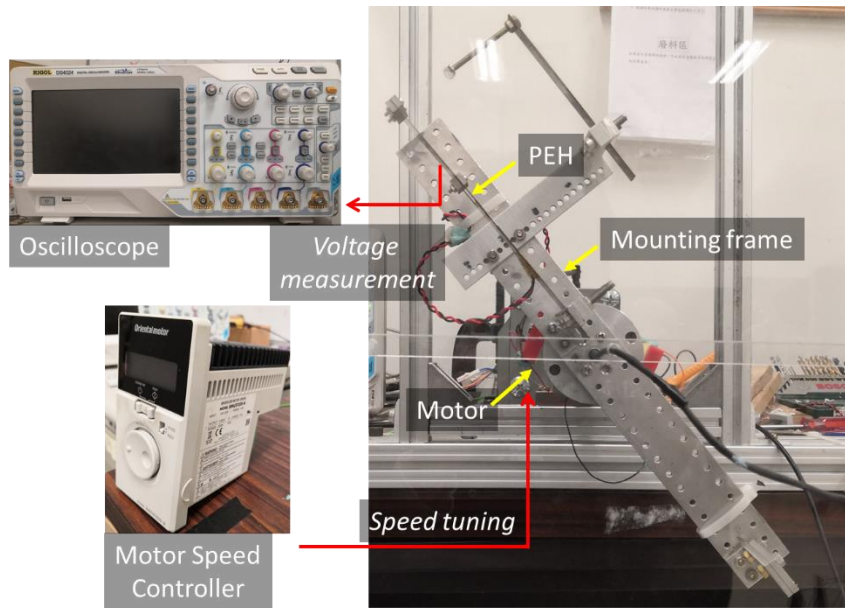


Fig. 10 Rotational experiment platform.

4. Results

In this chapter, the PEH is firstly examined with rotational excitation derived to validate the resonant frequency and fit the damping ratio. Additionally, some structure parameters will be modified to observe their effect on voltage, which include the Length of the main beam(L), the mass mounted on the main beam(M_1), and the mass mounted on the auxiliary beam(M_2). In Chapter 4.3 the impact impulse is introduced, and validated in 2 different impact positions. Finally, the magnetic force is introduced in Chap 4.4, validated in 2 different positions where the magnet force acts.

4.1. Rotational PEH under rotational excitation

Three prototypes of one basic PEH were tested under rotational excitation, as is shown in Fig. 11. The simulated resonant frequencies match the experimental ones well. By modifying experimental parameters such as L , M_1 and M_2 , when mode shape 1 resonates at lower/closer frequencies than mode shape 2 in Fig. 11 (a)(b), the curve of the first two voltage responses is a typical bimodal curve with an anti-resonance point. A notable difference between the simulation and experimental results is mostly reflected in the curve shape of resonance 2. The simulation result showed a softening effect while the experimental result was more like a hardening effect. The inward beam is theoretically supposed to be softened by the centrifugal force, but the simulation slightly overestimated the softening effect in this model. When mode shape 1 resonates at higher frequencies than mode shape 2 in Fig. 11 (c), we exchanged the terms of mode 1 and mode 2 in the simulation calculation, resulting in a nice fit without needing to change the damping ratio. The up sweep reached a higher peak than the down sweep and showed a hardening effect curve.

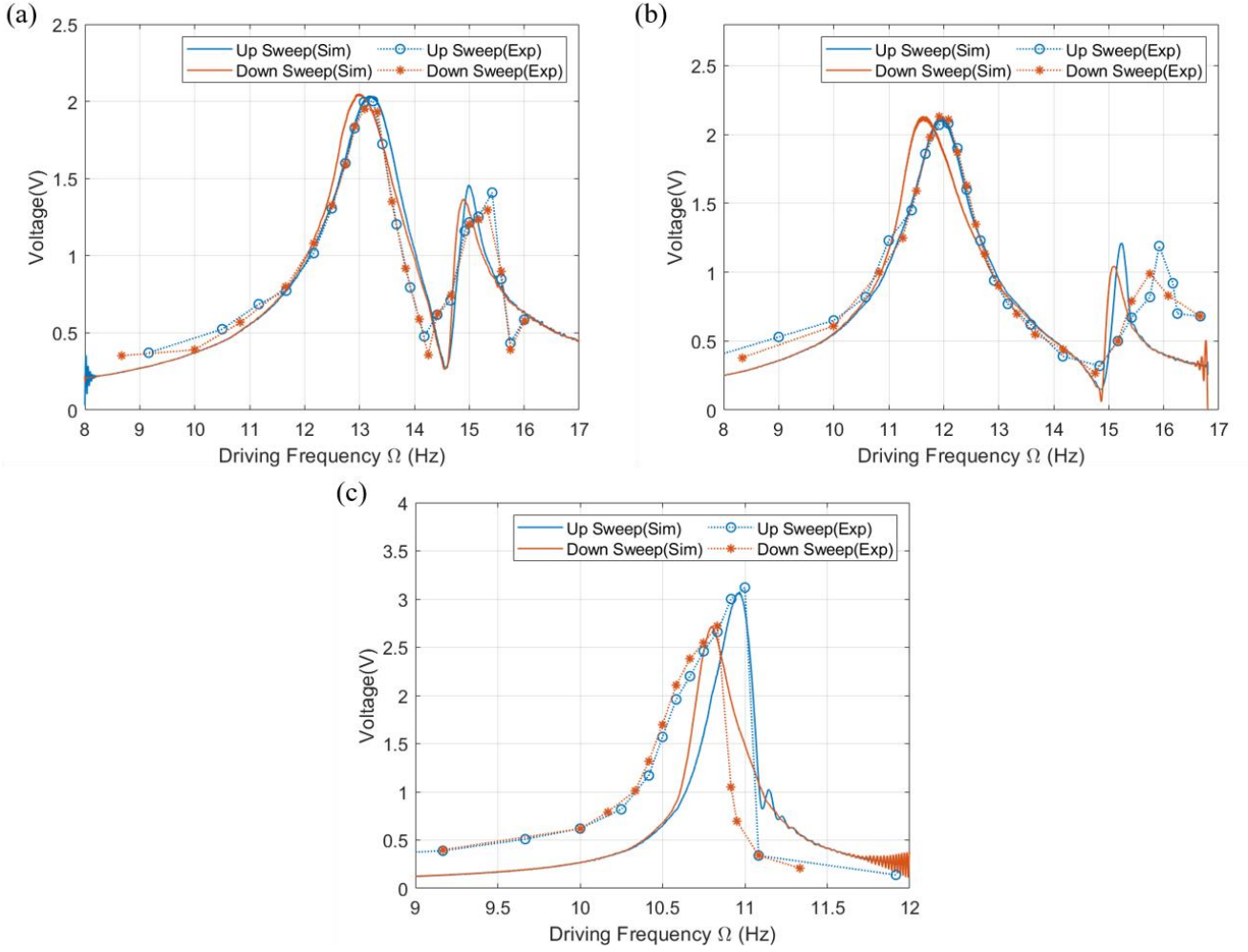


Fig. 11 Voltage responses of the PEH

- (a) mode shape 1 resonates at closer frequencies than mode shape 2;
 $M_1=2.42 \text{ g}$, $M_2=1.25 \text{ g}$, $\zeta_1=0.028$, $\zeta_2=0.034$;
- (b) mode shape 1 resonates at lower frequencies than mode shape 2;
 $M_1=3.42 \text{ g}$, $M_2=1.25 \text{ g}$, $\zeta_1=0.028$, $\zeta_2=0.034$;
- (c) mode shape 1 resonates at higher frequencies than mode shape 2;
 $M_1=2.42 \text{ g}$, $M_2=2.25 \text{ g}$, $\zeta_1=0.03$, $\zeta_2=0.035$.

4.2. Rotational PEH with different structure parameters

As is shown in Fig. 13, with the increase of L by 10 mm, the first and second resonance frequencies decreased by about 1 Hz, the peak of voltages decreased by about 0.5 V. In Table 2, the damping ratio changes with L , the power efficiency decreased significantly. As M_1 increases by 1g, the first resonance frequency decreases while the second resonance frequency increases, and the peak of voltage is reversed. In Table 2, different M_1 just has hardly any effect on the damping, the power efficiency is hardly affected. As M_2 increases by 1g, the resonance order of the mode shape 1 and 2 changes. the peak voltage increases significantly, but the frequency response width decreases severely, the resonance frequency of mode shape 1 decreases by 4-5 Hz, and the peak value of the mode shape 1 is too small to be recognized. As a result, the power generation efficiency decreases significantly.

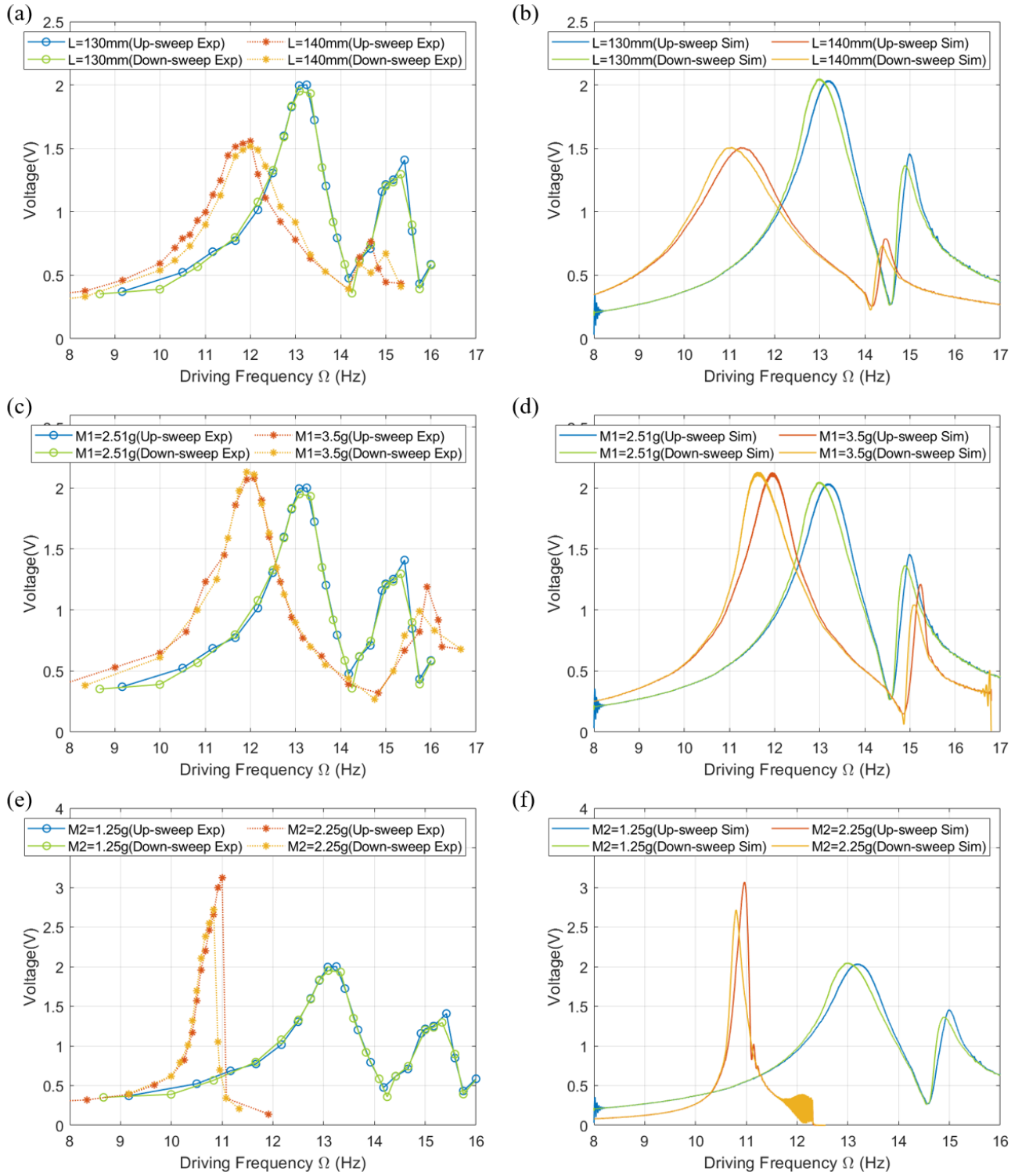


Fig. 12 Voltage responses of the PEH

- (a) different lengths of L (experiment); (b) different lengths of L (simulation);
 $\zeta_1=0.028$, $\zeta_2=0.034$ when $L=130\text{ mm}$; $\zeta_1=0.04$, $\zeta_2=0.045$ when $L=140\text{ mm}$;
(c) different weight of M_1 (experiment); (d) different weight of M_1 (simulation);
 $\zeta_1=0.028$, $\zeta_2=0.034$ when $M_1=2.42\text{ g}$; $\zeta_1=0.028$, $\zeta_2=0.034$ when $M_1=3.42\text{ g}$;
(e) different weight of M_2 (experiment); (f) different weight of M_2 (simulation);
 $\zeta_1=0.028$, $\zeta_2=0.034$ when $M_2=1.25\text{ g}$; $\zeta_1=0.03$, $\zeta_2=0.035$ when $M_2=2.25\text{ g}$.

Table 2 Comparison of power generation area with different parameters.

Parameters	Value	Sweep mode	Power generation area	Generation efficiency
Length of the main beam L	130 mm	up sweep	6.278e-3 mW·Hz	100%(Standard)
		down sweep	6.266e-3 mW·Hz	99.82%
	140 mm	up sweep	4.432e-3 mW·Hz	70.59%
		down sweep	4.434e-3 mW·Hz	70.63%
Weight of the mass at the main beam M_1	2.42 g	up sweep	6.864e-3 mW·Hz	100%(Standard)
		down sweep	6.729e-3 mW·Hz	98.03%
	3.42 g	up sweep	7.031e-3 mW·Hz	102.43%
		down sweep	7.103e-3 mW·Hz	103.48%
Weight of the mass at the auxiliary beam M_2	1.25 g	up sweep	6.150e-3 mW·Hz	100%(Standard)
		down sweep	6.090e-3 mW·Hz	99.03%
	2.25 g	up sweep	4.162e-3 mW·Hz	67.68%
		down sweep	3.011e-3 mW·Hz	48.95%

4.3. Rotational PEH with stopper

According to the results shown in Fig. 13, when the rest distance between the stopper and beam is 18.9 mm, curve around the first resonance frequency shows a hardening effect and the peak voltage of the second resonance decreases, the situation of the down sweep is a similar trend but with a smaller hardening effect. When the rest distance reduces to 14.4 mm, the hardening effect of resonance 1 increased. The effect also shown in the curve of resonance 2, which avoid the anti-resonance point and broaden the resonance2 range. The hardening effect is not notable during the down sweep. The results indicate that the proposed harvester can broaden the bandwidth by 1.17 Hz and 0.33 Hz at the first and second resonance frequencies, respectively. In Table 3, a stopper caused about 30% power loss during up sweep while up to 35% during down sweep.

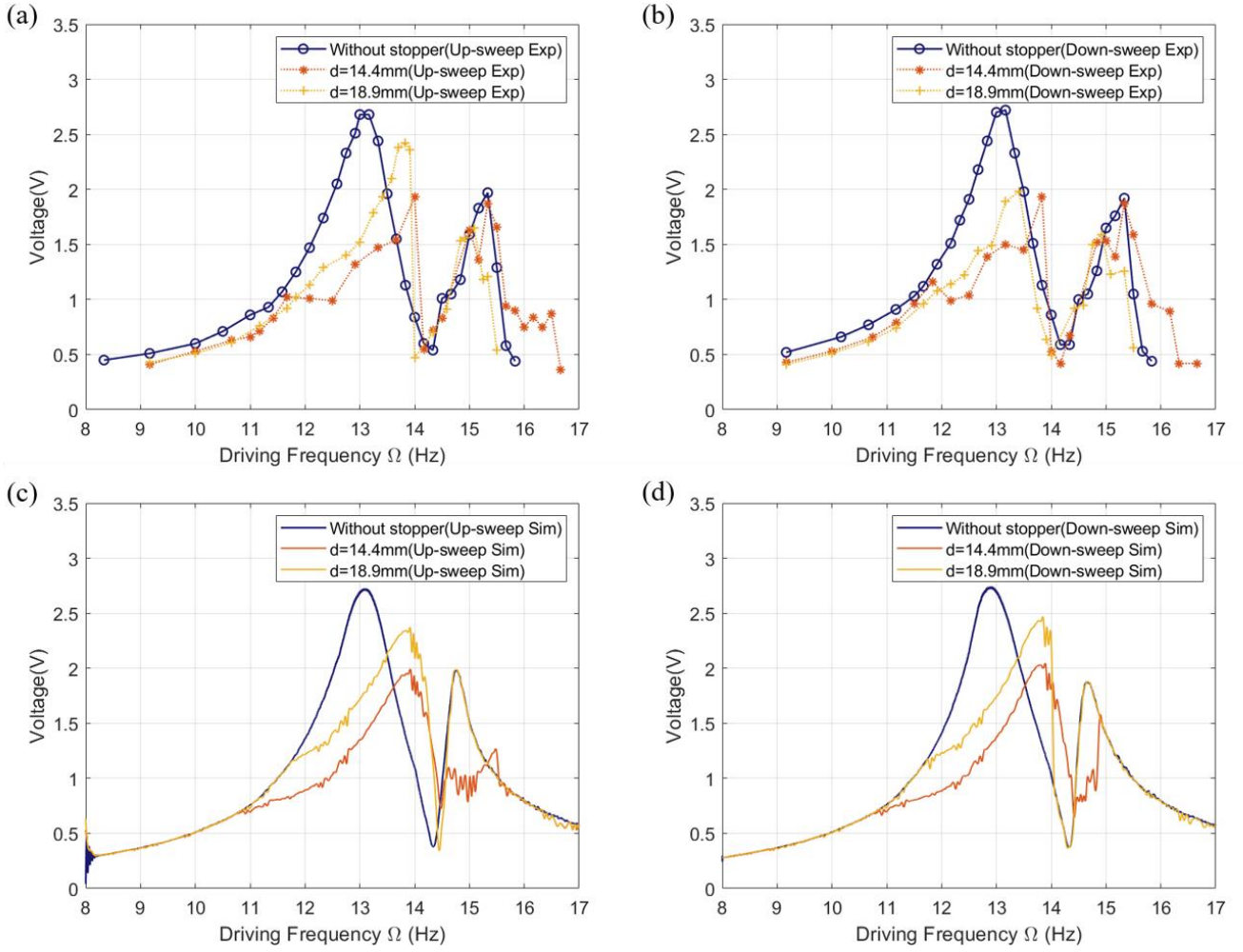


Fig. 13 Voltage responses of the PEH with stopper (main beam), $\zeta_1=0.028$, $\zeta_2=0.034$;

(a) up-sweep (experiment); (b) down-sweep (experiment);

(c) up-sweep (simulation); (d) down-sweep (simulation).

Table 3 Comparison of power generation area with a stopper on the main beam.

Parameters	Value	Sweep mode	Power generation area	Generation efficiency
Displacement of the gap	Without stopper	up sweep	12.54e-3 mW·Hz	100%(Standard)
		down sweep	12.41e-3 mW·Hz	98.94%
	14.4 mm	up sweep	8.74e-3 mW·Hz	69.68%
		down sweep	8.61e-3 mW·Hz	68.65%
	18.9 mm	up sweep	8.91e-3 mW·Hz	71.06%
		down sweep	8.15e-3 mW·Hz	64.99%

As depicted in Fig. 14, the curve of power response experiences a slight loss when $d=24.4$ mm. The peak voltage of resonance1 decreases mildly, while the peak voltage of resonance2 undergoes a significant decrease. However, the hardening effect is not noticeable. But the hardening effect becomes obvious when

d decreases to 15.4 mm, the bandwidth increases by 1 Hz and the peak of resonance2 decreases, the bandwidth of the up sweep is much higher than that of the down sweep. In Table 4, a stopper caused 20%-24% power loss during up sweep and barely any loss during down sweep.

We find that the collision occurs not only in mode shape 2, but it can also occur in mode shape 1 when d is small. $d=24.4\text{mm}$ and 15.4mm are different cases of whether the collision in mode shape 1 occurs, the hardening effect only appears when the collision occurs, we called this phenomenon collision threshold, and the threshold is 16.4mm by sim results in this study case. When the collision occurs, the effect will not affect the curve of resonance1 immediately, but affect on the curve of resonance2, as a result, the hardening effect graded changes rather than continuous, and so does a reverse growth of power efficiency.

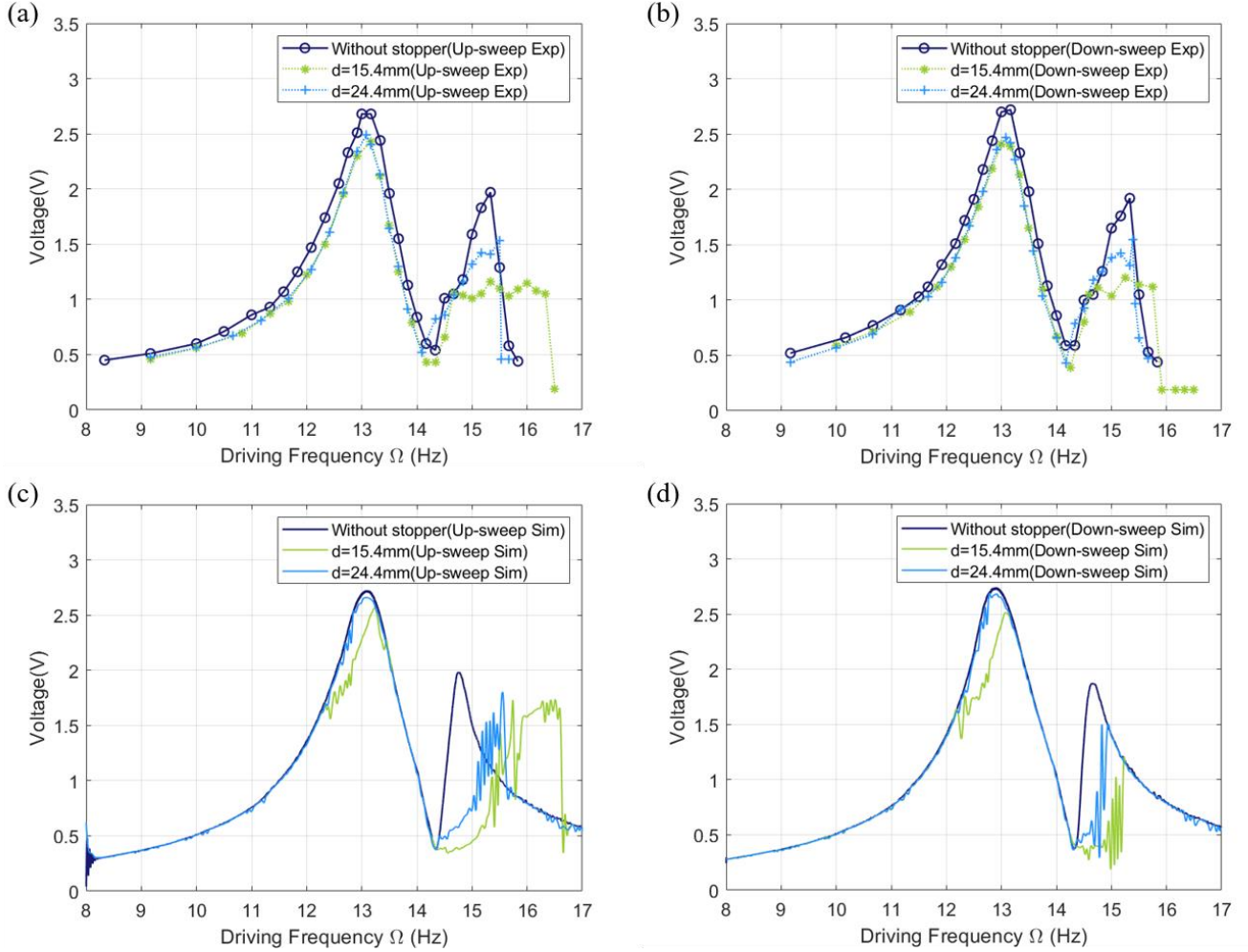


Fig. 14 Voltage responses of the PEH with stopper (auxiliary beam), $\zeta_1=0.028$, $\zeta_2=0.034$;

(a) up-sweep (experiment); (b) down-sweep (experiment);

(c) up-sweep (simulation); (d) down-sweep (simulation).

Table 4 Comparison of power generation area with a stopper on the auxiliary beam.

Parameters	Value	Sweep mode	Power generation area	Generation efficiency
Displacement of the gap	Without stopper	up sweep	12.54e-3 mW·Hz	100%(Standard)
	stopper	down sweep	12.41e-3 mW·Hz	98.94%

15.4 mm	up sweep	$9.92e-3 \text{ mW}\cdot\text{Hz}$	79.10%
	down sweep	$9.62e-3 \text{ mW}\cdot\text{Hz}$	76.73%
24.4 mm	up sweep	$9.86e-3 \text{ mW}\cdot\text{Hz}$	78.58%
	down sweep	$9.79e-3 \text{ mW}\cdot\text{Hz}$	78.09%

4.4. Rotational PEH with magnetic force

The results of the rotational PEH with main beam magnetic force are presented in Fig. 15, the voltage response curve of up sweep is a classic hardening effect and the bandwidth range increases, the simulation matches the experimental results, except for a small difference in the dropping point of the hardening curve. It is explained by the loss of energy, which increases with the distances decrease. As for the energy loss shown in Table 5, the gap distance does not show a significant difference

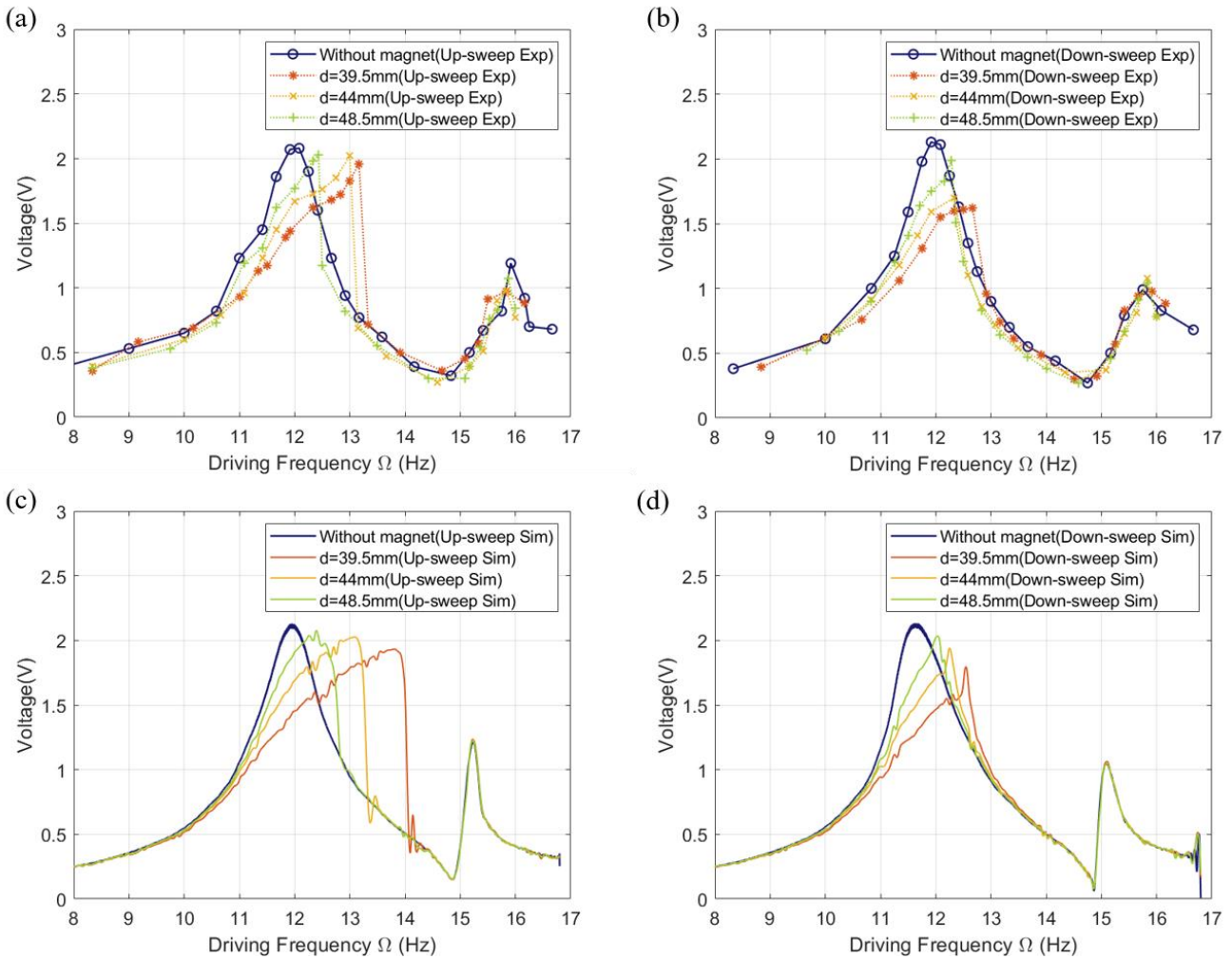


Fig. 15 Voltage responses of the PEH with magnetic force (main beam), $\zeta_1=0.026$, $\zeta_2=0.028$;

- (a) up-sweep (experiment); (b) down-sweep (experiment);
- (c) up-sweep (simulation); (d) down-sweep (simulation).

Table 5 Comparison of power generation area with magnets on the main beam.

Parameters	Value	Sweep mode	Power generation area	Generation efficiency
Displacement of the gap	Without magnets	up sweep	$7.37e-3 \text{ mW}\cdot\text{Hz}$	100%(Standard)
		down sweep	$7.43e-3 \text{ mW}\cdot\text{Hz}$	100.9%
	48.5 mm	up sweep	$5.66e-3 \text{ mW}\cdot\text{Hz}$	76.8%
		down sweep	$5.56e-3 \text{ mW}\cdot\text{Hz}$	75.4%
	44 mm	up sweep	$6.85e-3 \text{ mW}\cdot\text{Hz}$	93.0%
		down sweep	$5.23e-3 \text{ mW}\cdot\text{Hz}$	71.0%
	39.5 mm	up sweep	$6.85 \text{ e-3 mW}\cdot\text{Hz}$	92.9%
		down sweep	$5.43 \text{ e-3 mW}\cdot\text{Hz}$	73.6%

As is shown in Fig. 16, the trend of the magnetic force case matches the experiments. A notable difference is the peak results of $d=48.5 \text{ mm}$ and $d=53 \text{ mm}$ are close in experiments while different in simulation. This difference is explained by the additional force created by the magnet on the auxiliary beam, which interacts with the third part of the main beam, made of steel. This interaction results in an additional stable system and affects the results negatively. In Table 6, the efficiency loss is about 1/3 during up sweep and about 20% during down sweep.

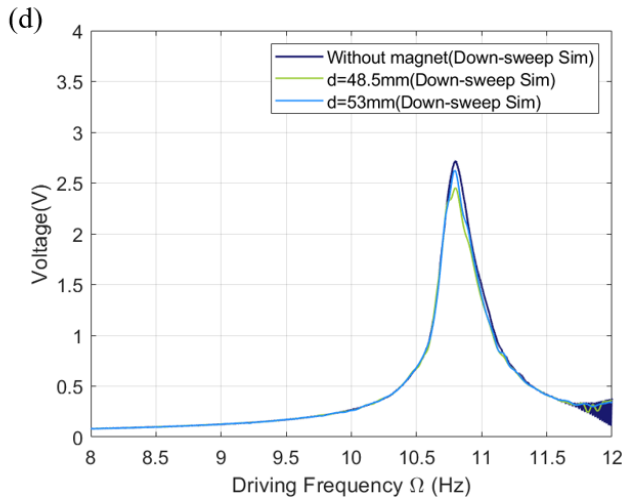
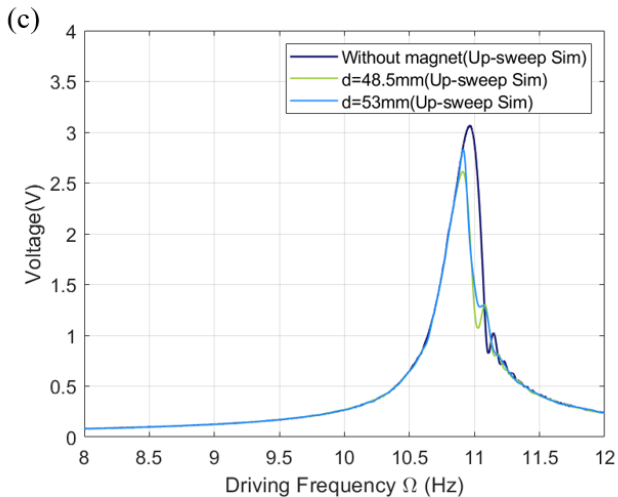
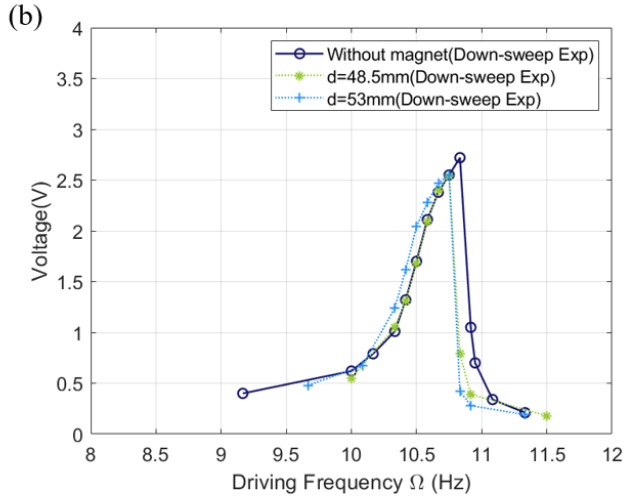
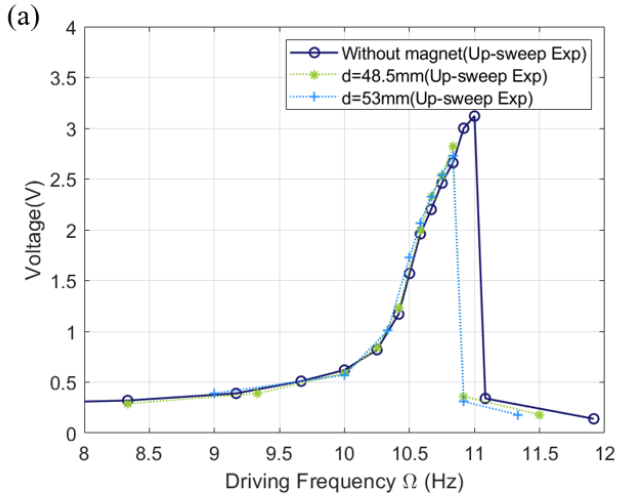


Fig. 16 Voltage responses of the PEH with magnetic force (auxiliary beam), $\zeta_1=0.03$, $\zeta_2=0.035$;

(a) up-sweep (experiment); (b) down-sweep (experiment);
(c) up-sweep (simulation); (d) down-sweep (simulation).

Table 6 Comparison of power generation area with magnets on the auxiliary beam.

Parameters	Value	Sweep mode	Power generation area	Generation efficiency
Displacement of the gap	Without magnets	up sweep	3.96e-3 mW·Hz	100%(Standard)
		down sweep	2.75e-3 mW·Hz	69.53%
	48.5 mm	up sweep	2.58e-3 mW·Hz	65.24%
		down sweep	2.06e-3 mW·Hz	52.11%
	53 mm	up sweep	2.60e-3 mW·Hz	65.63%
		down sweep	2.36e-3 mW·Hz	59.79%

5. Conclusion

In this paper, a two-degree-of-freedom cut-out beam PEH is studied. The PEH has two resonance frequencies and peaks in low frequency. First, we discuss 3 prototypes of one basic rotational PEH in which the mode shape 1 resonates at closer, lower and higher frequencies than mode shape 2. The effect of different structure parameters is also discussed. Furthermore, this study uses two types of nonlinear external force to broaden the bandwidth: the mechanical stopper with impulse force changes the rigidity of the system by collision, and the magnetic force changes the rigidity of the system in a non-contact way.

In this developed geometric nonlinear model, the limitation of small displacement vibration is removed. Generally, the simulation matches the results well. Compared to previous literature, the simulation results are much more precise for rotational energy harvesting. The impulse force and the magnetic force have an obvious effect in broadening the bandwidth. However, the power output observed in experiments decreases due to the hardening and softening effect of nonlinear force, as well as the associated damping. All cases cannot affect the curve near the anti-resonance point or connect the two resonance peaks.

In conclusion, the maximum power efficiency of the PEH with nonlinear force obtained in experiments is 93% (magnets at main beam); the maximum bandwidth increase in experiments is 1.17 Hz (resonance 1) + 0.33 Hz (resonance 2) (stopper at main beam); a local optimization of the PEH with stopper at auxiliary beam is a gap equals to the amplitude of auxiliary beam in resonance of mode shape 1.

CRedit authorship contribution statement

Xiang-Yu Li: Data curation, Investigation, Software, Validation, Visualization, Writing - original draft.

I-Chie Huang: Methodology, Software.

Wei-Jiun Su: Conceptualization, Methodology, Funding acquisition, Project administration, Resources, Supervision, Validation, Visualization, Writing - review & editing.

Acknowledgments

The authors gratefully acknowledge the financial support of the National Science and Technology Council of Taiwan under grant MOST 110-2221-E-002-141-MY3.

References

- [1] A. Erturk and D. J. Inman, "A distributed parameter electromechanical model for cantilevered piezoelectric energy harvesters," *Journal of vibration and acoustics*, vol. 130, no. 4, p. 041002, 2008.
- [2] A. Erturk and D. J. Inman, "An experimentally validated bimorph cantilever model for piezoelectric energy harvesting from base excitations," *Smart materials and structures*, vol. 18, no. 2, p. 025009, 2009.
- [3] M. Rafiee, F. Nitzsche, and M. Labrosse, "Dynamics, vibration and control of rotating composite beams and blades: A critical review," *Thin-Walled Structures*, vol. 119, pp. 795-819, 2017.
- [4] A. Yigit, R. Scott, and A. G. Ulsoy, "Flexural motion of a radially rotating beam attached to a rigid body," *Journal of Sound and Vibration*, vol. 121, no. 2, pp. 201-210, 1988.
- [5] L. Gu and C. Livermore, "Compact passively self-tuning energy harvesting for rotating applications," *Smart materials and structures*, vol. 21, no. 1, p. 015002, 2011.
- [6] F. Khameneifar, S. Arzanpour, and M. Moallem, "A piezoelectric energy harvester for rotary motion applications: Design and experiments," *IEEE/ASME Transactions on Mechatronics*, vol. 18, no. 5, pp. 1527-1534, 2012.
- [7] F. Khameneifar, M. Moallem, and S. Arzanpour, "Modeling and analysis of a piezoelectric energy scavenger for rotary motion applications," *Journal of vibration and acoustics*, vol. 133, no. 1, p. 011005, 2011.
- [8] J.-C. Hsu, C.-T. Tseng, and Y.-S. Chen, "Analysis and experiment of self-frequency-tuning piezoelectric energy harvesters for rotational motion," *Smart Materials and Structures*, vol. 23, no. 7, p. 075013, 2014.
- [9] X. Mei, Z. Wu, and S. Zhou, "The effect of centrifugal force on the dynamic performance of beam-type rotational energy harvesters," *The European Physical Journal Special Topics*, vol. 231, pp. 1383–1392, 2022.
- [10] W.-J. Su, J.-H. Lin, and W.-C. Li, "Analysis of a cantilevered piezoelectric energy harvester in different orientations for rotational motion," *Sensors*, vol. 20, no. 4, p. 1206, 2020.
- [11] Ö. Turhan and G. Bulut, "On nonlinear vibrations of a rotating beam," *Journal of Sound and Vibration*, vol. 322, no. 1-2, pp. 314-335, 2009.
- [12] Q. Gao *et al.*, "A rotating auxetic energy harvester for vehicle wheels," *Engineering Structures*, vol. 288, p. 116190, 2023.
- [13] K. Chen, S. Fang, Q. Gao, D. Zou, J. Cao, and W.-H. Liao, "Enhancing power output of piezoelectric energy harvesting by gradient auxetic structures," *Applied Physics Letters*, vol. 120, no. 10, p. 103901, 2022.

- [14] Q. Gao, Z. Ding, and W.-H. Liao, "Effective elastic properties of irregular auxetic structures," *Composite Structures*, vol. 287, p. 115269, 2022.
- [15] S. M. Hoseyni, M. Simsek, A. Aghakhani, E. Lefeuvre, and I. Basdogan, "Multimodal piezoelectric energy harvesting on a thin plate integrated with SSHI circuit: an analytical and experimental study," *Smart Materials and Structures*, vol. 32, no. 9, p. 095024, 2023.
- [16] S. Fang *et al.*, "Broadband energy harvester for low-frequency rotations utilizing centrifugal softening piezoelectric beam array," *Energy*, vol. 241, p. 122833, 2022.
- [17] W.-J. Su and C.-H. Tseng, "Design and Analysis of an Extended Simply Supported Beam Piezoelectric Energy Harvester," *Sensors*, vol. 23, no. 13, p. 5895, 2023.
- [18] X. Mei, R. Zhou, S. Fang, S. Zhou, B. Yang, and K. Nakano, "Theoretical modeling and experimental validation of the centrifugal softening effect for high-efficiency energy harvesting in ultralow-frequency rotational motion," *Mechanical Systems and Signal Processing*, vol. 152, p. 107424, 2021.
- [19] S. Kim *et al.*, "Propeller-based Underwater Piezoelectric Energy Harvesting System for an Autonomous IoT Sensor System," *Journal of the Korean Physical Society*, vol. 76, no. 3, pp. 251-256, 2020.
- [20] S. P. Machado, M. Febbo, J. M. Ramírez, and C. D. Gatti, "Rotational double-beam piezoelectric energy harvester impacting against a stop," *Journal of Sound and Vibration*, vol. 469, p. 115141, 2020.
- [21] J. Chen, X. Liu, H. Wang, S. Wang, and M. Guan, "Design and Experimental Investigation of a Rotational Piezoelectric Energy Harvester with an Offset Distance from the Rotation Center," *Micromachines*, vol. 13, no. 3, p. 388, 2022.
- [22] J. Kan, M. Zhang, S. Wang, Z. Zhang, Y. Zhu, and J. Wang, "A cantilevered piezoelectric energy harvester excited by an axially pushed wedge cam using repulsive magnets for rotary motion," *Smart Materials and Structures*, vol. 30, no. 6, p. 065009, 2021.
- [23] K. Fan, J. Liu, D. Wei, D. Zhang, Y. Zhang, and K. Tao, "A cantilever-plucked and vibration-driven rotational energy harvester with high electric outputs," *Energy Conversion and Management*, vol. 244, p. 114504, 2021.
- [24] X. Rui, Y. Zhang, Z. Zeng, G. Yue, X. Huang, and J. Li, "Design and analysis of a broadband three-beam impact piezoelectric energy harvester for low-frequency rotational motion," *Mechanical Systems and Signal Processing*, vol. 149, p. 107307, 2021.
- [25] A. Kumar, S. F. Ali, and A. Arockiarajan, "Exploring the benefits of an asymmetric monostable potential function in broadband vibration energy harvesting," *Applied Physics Letters*, vol. 112, no. 23, p. 233901, 2018.
- [26] M. Rezaei, R. Talebitooti, and W.-H. Liao, "Exploiting bi-stable magneto-piezoelastic absorber for simultaneous energy harvesting and vibration mitigation," *International Journal of Mechanical Sciences*, vol. 207, p. 106618, 2021.
- [27] M. Rezaei, R. Talebitooti, and W.-H. Liao, "Investigations on magnetic bistable PZT-based absorber for concurrent energy harvesting and vibration mitigation: Numerical and analytical

approaches," *Energy*, vol. 239, p. 122376, 2022.

- [28] M. Rezaei, R. Talebitooti, W.-H. Liao, and M. I. Friswell, "Integrating PZT layer with tuned mass damper for simultaneous vibration suppression and energy harvesting considering exciter dynamics: An analytical and experimental study," *Journal of Sound and Vibration*, vol. 546, p. 117413, 2023.
- [29] J. Kan, Y. Wu, S. Li, S. Wang, and Z. Zhang, "A tunable rotational energy harvester exploiting a flexible-clamping piezoelectric beam by deploying magnetic repulsive force," *Sensors and Actuators A: Physical*, vol. 353, p. 114198, 2023.
- [30] X. Mei, S. Zhou, Z. Yang, T. Kaizuka, and K. Nakano, "A tri-stable energy harvester in rotational motion: Modeling, theoretical analyses and experiments," *Journal of Sound and Vibration*, vol. 469, p. 115142, 2020.
- [31] X. Mei, S. Zhou, Z. Yang, T. Kaizuka, and K. Nakano, "Enhancing energy harvesting in low-frequency rotational motion by a quad-stable energy harvester with time-varying potential wells," *Mechanical Systems and Signal Processing*, vol. 148, p. 107167, 2021.
- [32] S. Fang *et al.*, "Comprehensive theoretical and experimental investigation of the rotational impact energy harvester with the centrifugal softening effect," *Nonlinear Dynamics*, vol. 101, no. 1, pp. 123-152, 2020.
- [33] S. Fang, S. Wang, S. Zhou, Z. Yang, and W.-H. Liao, "Exploiting the advantages of the centrifugal softening effect in rotational impact energy harvesting," *Applied Physics Letters*, vol. 116, no. 6, p. 063903, 2020.
- [34] H. Yu *et al.*, "A novel multimodal piezoelectric energy harvester with rotating-DOF for low-frequency vibration," *Energy Conversion and Management*, vol. 287, p. 117106, 2023.
- [35] V. Raja, M. Umopathy, G. Uma, and R. Usharani, "Performance enhanced piezoelectric rotational energy harvester using reversed exponentially tapered multi-mode structure for autonomous sensor systems," *Journal of Sound and Vibration*, vol. 544, p. 117429, 2023.
- [36] J.-X. Wang, W.-B. Su, J.-C. Li, and C.-M. Wang, "A rotational piezoelectric energy harvester based on trapezoid beam: Simulation and experiment," *Renewable Energy*, vol. 184, pp. 619-626, 2022.
- [37] S. Fang, K. Chen, Z. Lai, S. Zhou, and W.-H. Liao, "Analysis and experiment of auxetic centrifugal softening impact energy harvesting from ultra-low-frequency rotational excitations," *Applied Energy*, vol. 331, p. 120355, 2023.
- [38] J. Xing, S. Fang, X. Fu, and W.-H. Liao, "A rotational hybrid energy harvester utilizing bistability for low-frequency applications: Modelling and experimental validation," *International Journal of Mechanical Sciences*, vol. 222, p. 107235, 2022.
- [39] M. Perez, S. Boisseau, P. Gasnier, J. Willemin, M. Geisler, and J. Reboud, "A cm scale electret-based electrostatic wind turbine for low-speed energy harvesting applications," *Smart materials and structures*, vol. 25, no. 4, p. 045015, 2016.
- [40] S. Fang, J. Xing, K. Chen, X. Fu, S. Zhou, and W.-H. Liao, "Hybridizing piezoelectric and electromagnetic mechanisms with dynamic bistability for enhancing low-frequency rotational

energy harvesting," *Applied Physics Letters*, vol. 119, no. 24, p. 243903, 2021.

[41] G. Akoun and J.-P. Yonnet, "3D analytical calculation of the forces exerted between two cuboidal magnets," *IEEE Transactions on magnetics*, vol. 20, no. 5, pp. 1962-1964, 1984.

Appendix

A. Force Balance of a Beam Unit

As is shown in Fig. 17, the balance of force on length units is analyzed, which divided in the direction perpendicular to the axis of rotation, which is shown as direction Z, and parallel to the axis of rotation, which is shown as direction X. where F is a force per unit area in the direction of \hat{i} , Q is a force per unit area in the direction of \hat{n} ; α is angle of beam unit during vibration.

$$\begin{cases} \frac{\partial}{\partial x_i} [F_i \cos(\alpha_i(x_i, t))] - \frac{\partial}{\partial x_i} [Q_i \sin(\alpha_i(x_i, t))] = -m_i \left[\frac{\partial^2 u_i(x_i, t)}{\partial t^2} - \Omega^2 (u_i(x_i, t) - x_i - R_i) \right] + m_i g \cos \Omega t & i = 1, 2, 3 \\ \frac{\partial}{\partial x_4} [F_4 \cos(\alpha_4(x_4, t))] - \frac{\partial}{\partial x_4} [Q_4 \sin(\alpha_4(x_4, t))] = -m_4 \left[\frac{\partial^2 u_4(x_4, t)}{\partial t^2} - \Omega^2 (u_4(x_4, t) - x_4 - R_4) \right] - m_4 g \cos \Omega t \end{cases} \quad (44)$$

$$\begin{cases} \frac{\partial}{\partial x_i} [F_i \sin(\alpha_i(x_i, t))] + \frac{\partial}{\partial x_i} [Q_i \cos(\alpha_i(x_i, t))] = -m_i \left[\frac{\partial^2 w_i(x_i, t)}{\partial t^2} - \Omega^2 w_i(x_i, t) \right] - m_i g \sin \Omega t & i = 1, 2, 3 \\ \frac{\partial}{\partial x_4} [F_4 \sin(\alpha_4(x_4, t))] + \frac{\partial}{\partial x_4} [Q_4 \cos(\alpha_4(x_4, t))] = -m_4 \left[\frac{\partial^2 w_4(x_4, t)}{\partial t^2} - \Omega^2 w_4(x_4, t) \right] + m_4 g \sin \Omega t \end{cases} \quad (45)$$

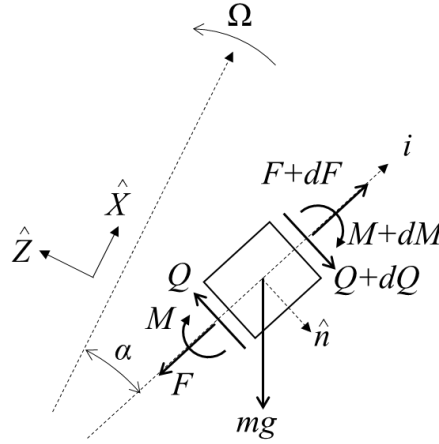


Fig. 17 Balance of force on beam body unit

B. Force Balance on Boundaries of Different Beam Sections

As is shown in Fig. 18, the balance of force on the boundary of different beam sections is eqns.(46)-(47).

$$\begin{cases}
-F_i \cos(\alpha_i(L_i, t)) + Q_i \sin(\alpha_i(L_i, t)) = -F_{i+1} \cos(\alpha_{i+1}(0, t)) + Q_{i+1} \sin(\alpha_{i+1}(0, t)) & i = 1, 2 \\
-F_3 \cos(\alpha_3(L_3, t)) + Q_3 \sin(\alpha_3(L_3, t)) - F_4 \cos(\alpha_4(0, t)) + Q_4 \sin(\alpha_4(0, t)) \\
= -Mt_3 \left[\frac{\partial^2 u_3(L_3, t)}{\partial t^2} - \Omega^2 (u_3(L_3, t) - L_3 - R_3) \right] + Mt_3 g \cos \Omega t \\
-F_4 \cos(\alpha_4(L_4, t)) + Q_4 \sin(\alpha_4(L_4, t)) + Mt_4 g \cos \Omega t = -Mt_4 \left[\frac{\partial^2 u_4(L_4, t)}{\partial t^2} - \Omega^2 (w_4(L_4, t) - L_4 - R_4) \right]
\end{cases} \quad (46)$$

$$\begin{cases}
-F_i \sin(\alpha_i(L_i, t)) - Q_i \cos(\alpha_i(L_i, t)) = -F_{i+1} \sin(\alpha_{i+1}(0, t)) - Q_{i+1} \cos(\alpha_{i+1}(0, t)) & i = 1, 2 \\
-F_3 \sin(\alpha_3(L_3, t)) - Q_3 \cos(\alpha_3(L_3, t)) - F_4 \sin(\alpha_4(0, t)) - Q_4 \cos(\alpha_4(0, t)) \\
= Mt_3 \left[\frac{\partial^2 w_3(L_3, t)}{\partial t^2} - \Omega^2 w_3(L_3, t) \right] - Mt_3 g \sin \Omega t \\
-F_4 \sin(\alpha_4(L_4, t)) - Q_4 \cos(\alpha_4(L_4, t)) - Mt_4 g \sin \Omega t = Mt_4 \left[\frac{\partial^2 w_4(L_4, t)}{\partial t^2} - \Omega^2 w_4(L_4, t) \right]
\end{cases} \quad (47)$$

(a)

(b)

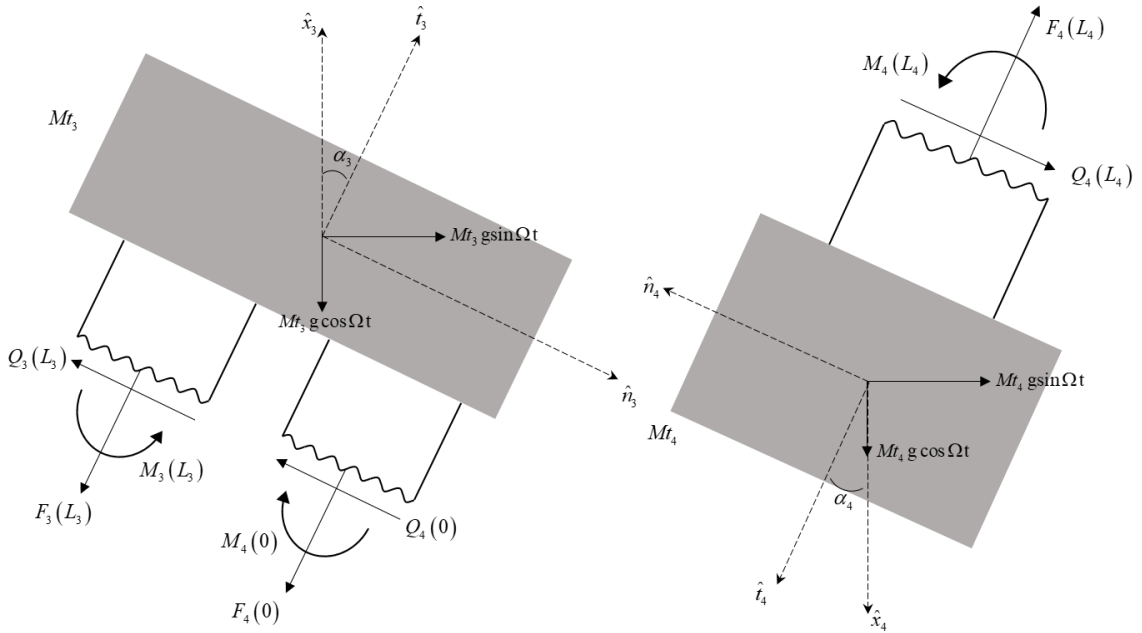


Fig. 18 Force equilibrium at boundaries (a) at M_1 (b) at M_2

C. Action Term of Mechanical Vibration Equation

$$Mb_{jk} = \sum_{i=1}^4 \int_0^{L_i} \phi_{ik}(x_i) m_i \phi_{ij}(x_i) dx_i + \phi_{ik}(x_i) Mt_i \phi_{ij}(x_i) \Big|_{x_i=L_i} \quad (48)$$

$$Kb_{jk} = \sum_{i=1}^4 \int_0^{L_i} \frac{d^2 \phi_{ik}(x_i)}{dx_i^2} YI_i \frac{d^2 \phi_{ij}(x_i)}{dx_i^2} dx_i \quad (49)$$

$$Ks_{jk} = \sum_{i=1}^2 \int_0^{L_i} \frac{d\phi_{ik}(x_i)}{dx_i} [fc_i(x_i) + fc_{i+1}(0)] \frac{d\phi_{ij}(x_i)}{dx_i} dx_i \\ + \int_0^{L_3} \frac{d\phi_{3k}(x_3)}{dx_3} [fc_3(x_3) - fc_4(0)] \Omega^2 \frac{d\phi_{3j}(x_3)}{dx_3} dx_3 + \int_0^{L_4} \frac{d\phi_{4k}(x_4)}{dx_4} fc_4(x_4) \Omega^2 \frac{d\phi_{4j}(x_4)}{dx_4} dx_4 \quad (50)$$

$$Kg_{jk} = \sum_{i=1}^2 \int_0^{L_i} \frac{d\phi_{ik}(x_i)}{dx_i} [fg_i(x_i) - fg_{i+1}(0)] \frac{d\phi_{ij}(x_i)}{dx_i} dx_i \\ + \int_0^{L_3} \frac{d\phi_{3k}(x_3)}{dx_3} [fg_3(x_3) + fg_4(0)] \Omega^2 \frac{d\phi_{3j}(x_3)}{dx_3} dx_3 - \int_0^{L_4} \frac{d\phi_{4k}(x_4)}{dx_4} fg_4(x_4) \Omega^2 \frac{d\phi_{4j}(x_4)}{dx_4} dx_4 \quad (51)$$

$$Rs_{jk} = \sum_{i=1}^4 \int_0^{L_i} \frac{\partial \phi_{ik}(x_i, t)}{\partial x_i} YI_i \frac{\partial \phi_{ij}(x_i, t)}{\partial x_i} \frac{\partial \left(\frac{\partial \phi_{ij}(x_i, t)}{\partial x_i} \frac{\partial^2 \phi_{ij}(x_i, t)}{\partial x_i^2} \right)}{\partial x_i} dx_i \quad (52)$$

$$Kn_{jk} = \sum_{i=1}^2 \int_0^{L_i} \frac{d\phi_{ik}(x_i)}{dx_i} [\overline{fn}_i(x_i) + \overline{fn}_{i+1}(0)] \frac{d\phi_{ij}(x_i)}{dx_i} dx_i \\ + \int_0^{L_3} \frac{d\phi_{3k}(x_3)}{dx_3} [\overline{fn}_3(x_3) - \overline{fn}_4(0)] \Omega^2 \frac{d\phi_{3j}(x_3)}{dx_3} dx_3 + \int_0^{L_4} \frac{d\phi_{4k}(x_4)}{dx_4} \overline{fn}_4(x_4) \Omega^2 \frac{d\phi_{4j}(x_4)}{dx_4} dx_4 \quad (53)$$

where $\overline{fn}_i(x_i)$ is the real field of $fn_i(x_i, t)$.

$$F_j = \sum_{i=1}^3 \left[\int_0^{L_i} \phi_{ij}(x_i) g dx_i + \phi_{ij}(L_i) Mt_i g \right] - \int_0^{L_4} \phi_{4j}(x_4) g dx_4 - \phi_{4j}(x_4) Mt_4 g \Big|_{x_i=L_i} \quad (54)$$